Int J Earth Sci (Geol Rundsch) (2016) 105:1985–2012
DOI 10.1007/s00531-016-1293-4

ORIGINAL PAPER

Structure and U–Pb zircon geochronology of an Alpine nappe stack telescoped by extensional detachment faulting (Kulidzhik area, Eastern Rhodopes, Bulgaria)

Neven Georgiev[1] · Nikolaus Froitzheim[2] · Zlatka Cherneva[3] · Dirk Frei[4] · Valentin Grozdev[5] · Silke Jahn-Awe[2] · Thorsten J. Nagel[6]

Received: 7 July 2015 / Accepted: 25 December 2015 / Published online: 19 January 2016

Abstract The Rhodope Metamorphic Complex is a stack of allochthons assembled during obduction, subduction, and collision processes from Jurassic to Paleogene and overprinted by extensional detachment faults since Middle Eocene. In the study area, the following nappes occur in superposition (from base to top): an orthogneiss-dominated unit (Unit I), garnet-bearing schist with amphibolite and serpentinite lenses (Unit II), greenschist, phyllite, and calcschist with reported Jurassic microfossils (Unit III), and muscovite-rich orthogneiss (Unit IV). U–Pb dating of zircons from a K-feldspar augengneiss (Unit I) yielded a protolith age of ca. 300 Ma. Garnet-bearing metasediment from Unit II yielded an age spectrum with distinct populations between 310 and 250 Ma (detrital), ca. 150 Ma, and ca. 69 Ma (the last two of high-grade metamorphic origin). An orthogneiss from Unit IV yielded a wide spectrum of ages. The youngest population gives a concordia age of 581 ± 5 Ma, interpreted as the age of the granitic protolith. Unit I represents the Lower Allochthon (Byala Reka-Kechros Dome), Unit II the Upper Allochthon (Krumovitsa-Kimi Unit), Unit III the Uppermost Allochthon (Circum-Rhodope Belt), and Unit IV a still higher, far-travelled unit of unknown provenance. Telescoping of the entire Rhodope nappe stack to a thickness of only a few 100 m is due to Late Eocene north directed extensional shearing along the newly defined Kulidzhik Detachment which is part of a major detachment system along the northern border of the Rhodopes. Older top-to-the south mylonites in Unit I indicate that Tertiary extension evolved from asymmetric (top-to-the-south) to symmetric (top-to-the-south and top-to-the-north), bivergent unroofing.

Keywords Rhodope · Zircon dating · Tectonics · Metamorphic core complex · Detachment fault

Electronic supplementary material The online version of this article (doi:10.1007/s00531-016-1293-4) contains supplementary material, which is available to authorized users.

✉ Neven Georgiev
neven@gea.uni-sofia.bg

Zlatka Cherneva
cherneva@gea.uni-sofia.bg

1 Department of Geology, Paleontology and Fossil Fuels, Sofia University St. Kliment Ohridski, 15 Tzar Osvoboditel Blv., 1000 Sofia, Bulgaria

2 Steinmann-Institut, Universität Bonn, Poppelsdorfer Schloss, 53115 Bonn, Germany

3 Department of Mineralogy, Petrology and Economic Geology, Sofia University St. Kliment Ohridski, 15 Tzar Osvoboditel Blv., 1000 Sofia, Bulgaria

4 Central Analytical Facility and Department of Earth Sciences, Stellenbosch University, Matieland 7602, South Africa

5 Geological Institute of the Bulgarian Academy of Sciences, 24 Acad Georgi Bonchev Str., 1113 Sofia, Bulgaria

6 Department of Geoscience, Aarhus University, Hoegh-Guldbergs Gade 2, 8000 Århus C, Denmark

Introduction

The Rhodope Metamorphic Complex (Fig. 1) is a key element for the tectonic and palaeogeographic reconstruction of the Alpine orogeny in the Balkan Peninsula and Eastern Mediterranean. Subduction of continental crust is recorded by the occurrence of metamorphic microdiamond in gneisses of the Rhodopes (Mposkos and Kostopoulos 2001; Perraki et al. 2006; Schmidt

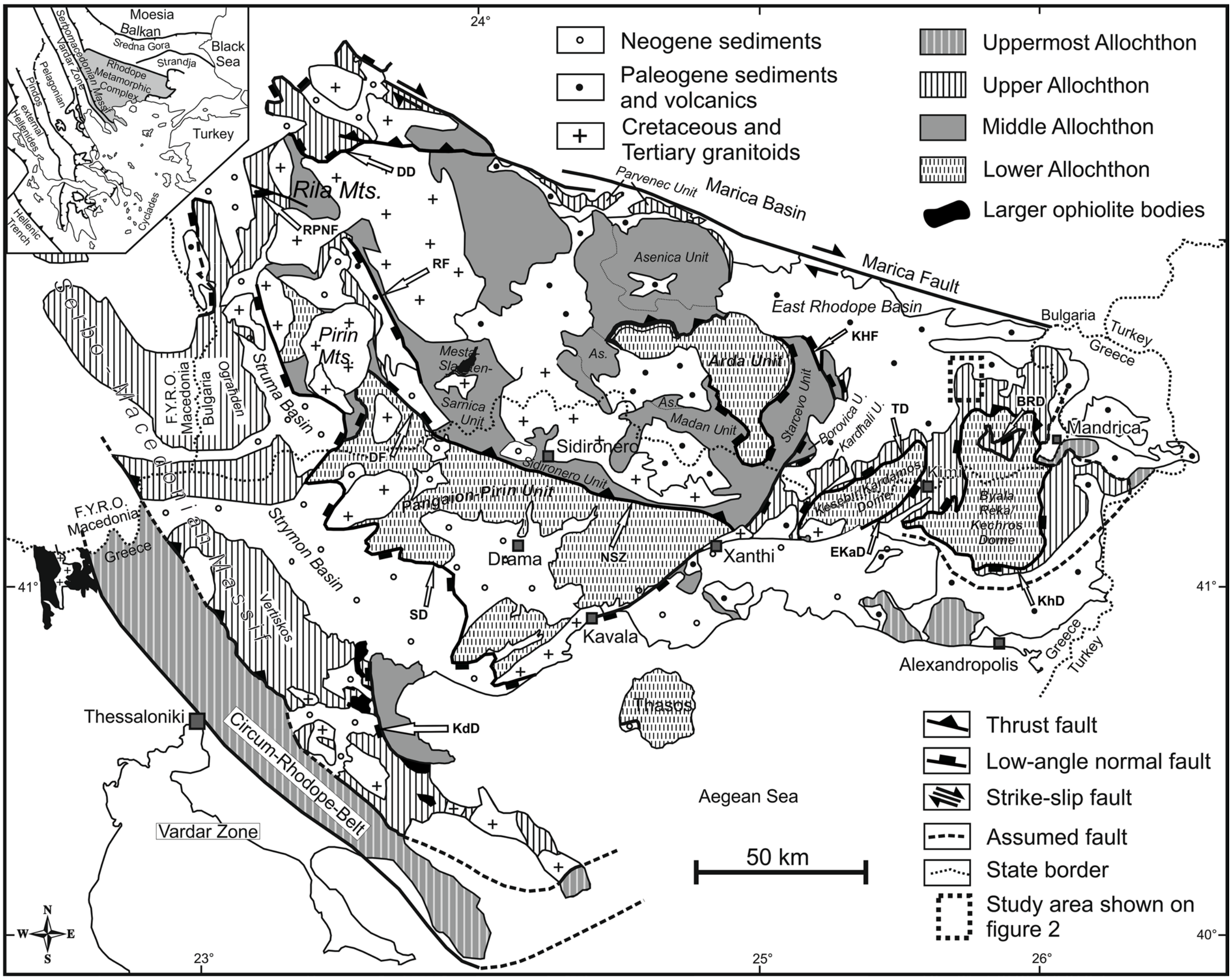

Fig. 1 Tectonic map of the Rhodope Metamorphic Complex (modified after Burg et al. 1996; Ricou et al. 1998; Bonev 2006b; Dixon and Dimitriadis 1984): *BRD* Byala reka Detachment, *KhD* Kehros Detachment, *TD* Tokachka Detachment, *EKaD* East Kardamos Detachment, *KHF* Kyuse-Hasanlartepsi Fault, *DD* Dzherman Detachment, *RPNF* Rila-Pastra Normal Fault, *RF* Ribnovo Fault, *DF* Dobrotino Fault, *KdD* Kerdilion Detachment, *DS* Strymon Detachment, *NSZ* Nestos Shear Zone

et al. 2010). Structural studies demonstrated Alpine thrust imbrication as well as rollback-related crustal extension, leading to the formation of extensional core complexes (e.g. Burg et al. 1990; Dinter 1998; Burchfiel et al. 2003; Bonev et al. 2006a; Brun and Sokoutis 2007; Jahn-Awe et al. 2010; Nagel et al. 2011). Geochronology suggests that there were several episodes of subduction-related high- to ultrahigh-pressure metamorphism, with ages ranging from Early Jurassic to Eocene (e.g. Liati 2005; Bauer et al. 2007; Kirchenbaur et al. 2012; Liati et al. 2015). In order to reconstruct the complicated tectonic history of the Rhodopes, it is of prime importance to understand the nature of tectonic contacts, i.e. to distinguish between compression-related thrusts and extension-related low-angle normal faults. In the present article, we describe the geological situation in the Kulidzhik River area of the eastern Rhodopes, where four tectonic units occur in superposition. Previous tectonic interpretations of the area were based on structural observations, lithological correlations, two $^{40}Ar–^{39}Ar$ white mica ages (Bonev et al. 2010a), and the finding of fossils in one of the units (Boyanov and Lipman 1973; Boyanov et al. 1990). The tectonic contacts were either interpreted as thrusts (Boyanov 1969; Bonev 2006a) or detachment faults (Ivanov 1998; Sarov et al. 2008). Here, we present structural observations from field work and thin sections as well as U–Pb zircon data from three samples, obtained by laser ablation inductively coupled plasma mass spectrometry (LA-ICPMS). Based on these and the published data, we propose a partially new tectonic interpretation in which the importance of extensional deformation is emphasised.

Regional setting

The Rhodopes represent a complicated Alpine tectonic edifice, composed of metamorphic nappes that were assembled during a protracted tectono-metamorphic history from Late Jurassic to Latest Eocene. The metamorphic nappes are in an overall flat-lying position and partly separated by thrusts, partly—and more often—by low-angle extensional detachment faults. Depending on the particular structural position, different nappes are intruded by Cretaceous to Tertiary granitoid plutons. Twice, at the end of the nappe stacking in the Eocene–Oligocene, and a second time in the Miocene, the Rhodope edifice was affected and reshaped by regional scale-extensional tectonics. This led to the exhumation of high-grade metamorphic units (including migmatites and eclogites) in several large domes and to the formation of Palaeogene to Neogene supra-detachment basins. Several slightly differing subdivision schemes have been proposed for the metamorphic nappes (Ricou et al. 1998; Dimov et al. 2000; Sarov et al. 2010; Janák et al. 2011; Burg 2012). We use the subdivision into four nappe systems or allochthons (Janák et al. 2011; Pleuger et al. 2011), based mainly on the age of the pervasive deformation, the degree and age of metamorphism, and the age of the oldest overlying sediments (Fig. 1). These ages generally increase from the Lower through the Middle and Upper to the Uppermost Allochthon.

The Lower Allochthon occurs in four dome-shaped core complexes (Pangaion-Pirin, Arda, Kesebir-Kardamos, Byala Reka-Kechros). It consists mainly of orthogneisses derived from Carboniferous to Permian granitoids (e.g. von Quadt and Peytcheva 1995; Peytcheva and von Quadt 1995; Liati and Gebauer 1999; Arkadakskiy et al. 2003; Cherneva et al. 2003; Ovtcharova et al. 2002; Peytcheva et al. 2004; Turpaud and Reischmann 2010). In the Pangaion-Pirin Dome, the gneisses are associated with large volumes of marble. Migmatisation affected the Lower Allochthon in the Arda dome at ~38 Ma (Peytcheva et al. 2004 and references therein). The migmatisation of the gneiss core of the Kesebir-Kardamos dome (Bonev 2004; Sarov et al. 2007) has not yet been dated. No migmatites have been reported so far within the cores of the Pangaion-Pirin and Byala Reka-Kechros Domes. In the Bulgarian part of the Eastern Rhodopes, the gneisses of the Lower Allochthon are termed Kesebir Lithotectonic Unit and Byala reka Lithotectonic Unit (Sarov et al. 2008, 2010) or lower high-grade basement unit (Bonev et al. 2010b).

The orthogneisses of the Lower Allochthon in the core of Byala Reka-Kechros Dome, close to our study area, followed a clockwise P–T path (Macheva 1998) including (1) a high pressure/low temperature (HP/LT) stage at 1.3 GPa and ~450 °C, related to crustal thickening during continent collision, (2) a stage between 0.9 and 0.3 GPa and ~550 °C, related to unroofing of the dome, and (3) a LP/LT stage at 0.3–0.2 GPa and ~400 °C preceding final cooling of the rocks. Similar conditions (1.4–1.55 GPa, min 550 °C) were determined for the peak-pressure stage in the Greek part of the dome (Mposkos 1989). $^{40}Ar/^{39}Ar$ laser probe dating of white mica yielded cooling ages of ca. 42–37 Ma for mica porphyroclasts and ~36 Ma for fine-grained, syn-kinematic mica (Lips et al. 2000). A more detailed $^{40}Ar/^{39}Ar$ study showed that the core of Byala Reka-Kechros Dome cooled below 350–300 °C between 35.5 and 38 Ma (Bonev et al. 2010b).

In the Western and Central Rhodopes, the Lower Allochthon is overlain by the Middle Allochthon comprising orthogneisses, often derived from Late Jurassic to Early Cretaceous calc-alkaline granitoids, mixed with metaophiolites. Eocene eclogite-facies metamorphism has been dated in the boundary zone between the Lower and Middle Allochthon (Liati 2005; Kirchenbaur et al. 2012). In the Eastern Rhodopes, units representative of the Middle Allochthon have not yet been identified with certainty.

The Upper Allochthon is dominated by gneisses but also comprises mafic and ultramafic metaophiolites as well as marbles and schists. It experienced HP and UHP metamorphism during the Jurassic and Cretaceous (e.g. Kirchenbaur et al. 2012; Liati et al. 2015). In contrast to the Lower and Middle allochthons which were intensely deformed and metamorphosed in the Palaeogene, the tectonometamorphic evolution of the Upper Allochthon was largely finished at the end of the Cretaceous, as can be seen from ca. 62 Ma old, crosscutting and little-deformed pegmatites (Liati et al. 2002) and 69–70 Ma old, discordant granite plutons (Marchev et al. 2006). The Upper Allochthon mainly occurs in the Eastern Rhodopes, along the northern border of the Central and Western Rhodopes, and in the Rila, Pirin, and Serbo-Macedonian massifs further west. In the Bulgarian part of the Eastern Rhodopes, the rocks of the Upper Allochthon are termed Krumovitsa Lithotectonic Unit (Sarov et al. 2008, 2010) or Upper high-grade basement unit (Bonev et al. 2010c). On the Greek side, the Upper Allochthon includes the Kimi Unit where diamond-bearing gneisses occur (Mposkos and Kostopoulos 2001; Perraki et al. 2006). $^{40}Ar/^{39}Ar$ muscovite dating of metapelitic schist from a klippe of Upper Allochthon located in the Byala Reka-Kechros dome shows that it cooled down through ~350 °C at ~39 Ma (Mukasa et al. 2003).

The Uppermost Allochthon, also termed Circum-Rhodope Triassic-Jurassic Tectonic Zone (Jaranoff 1960) or Circum-Rhodope Belt (Kauffmann et al. 1976), consists of arc- and backarc-related ophiolites and sedimentary rocks. The ophiolites are Mesozoic in age and the sedimentary rocks range from Triassic to Cretaceous. The rocks of the Uppermost Allochthon were partly metamorphosed in the greenschist and locally blueschist-facies already in the

Late Jurassic; younger sediments are unmetamorphosed (Michard et al. 1994). In the Bulgarian part of the Eastern Rhodopes, the Uppermost Allochthon corresponds to the phyllite-schist section of the Mandritsa Lithotectonic Unit (Sarov et al. 2008, 2010) or Low-grade Mesozoic unit" (Bonev et al. 2010c).

Tectonic units in the study area

The metamorphic rocks of the Kulidzhik area are located north of the Byala Reka-Kechros dome in a separate, isolated outcrop area where incision by the Arda River, the small river Kulidzhik, and its tributaries has removed the Paleogene sedimentary and volcanic cover (Fig. 2). The metamorphic rocks form subhorizontal, slightly folded lithological units.

Unit I

The lowermost unit (Unit I) is part of the Lower Allochthon of Janák et al. (2011). It is formed by orthogneiss, partly with augen structure, cropping out in an isolated area north and northwest of the village Bryagovets (Figs. 2, 3a). Foliation-parallel amphibolite lenses also occur in this unit. A lens of serpentinised ultramafic rock is exposed on both sides of the Kulidzhik River east of Bryagovets; this body appears to belong to the uppermost part of Unit I or to be situated at the boundary between units I and II. The boundary with the overlying Unit II represents a top-to-the-north (in the following abbreviated "top-north"), greenschist facies shear zone that was previously described as the Bryagovets-Brusevtsi detachment fault (Ivanov 1998; Sarov et al. 2008).

Unit II

This unit corresponds to the Upper Allochthon of Janák et al. (2011) and comprises garnet-chlorite-mica schist as the predominant rock type, amphibolite, thin layers of marble, and serpentinised ultramafic rocks (Fig. 2). The unit is pervasively overprinted by deformation under greenschist facies conditions. However, in the structurally lower part of Unit II along the Kulidzhik River near Bryagovets, an earlier, higher-grade fabric still occurs (Fig. 4). Garnet is preserved in this area, whereas higher up, it is partly or completely chloritised. Structurally upwards, Unit II is increasingly overprinted by greenschist facies mylonitic and, towards the top, cataclastic deformation. The structural overprinting is accompanied by upward-increasing chloritization of the rock, making it difficult to distinguish from the overlying greenschists of Unit III. The contact between units II and III is tectonic, marked by a layer of cataclasite (Fig. 3b).

Unit III

This unit is interpreted as a part of the Circum-Rhodope Belt (Bonev et al. 2010a), i.e. the Uppermost Allochthon. The unit comprises meta-volcanic greenschist, phyllite, and calcschist (Fig. 2). The greenschist is mostly found at the base of the unit. The metamorphic grade does not exceed the greenschist facies; we did not find garnet in this unit. The garnet-bearing rocks described by Bonev et al. (2010a), belong in our interpretation to the underlying Unit II. Unit III is of variable thickness between 0 and ca. 200 m. Boyanov and Lipman (1973) found microfossils in anchimetamorphic sediments in the upper part of Unit III, which they identified as Early Cretaceous. Tikhomirova et al. (1988) restudied the fossils dated by Boyanov and Lipman (1973) and modified the age into Early Jurassic. Boyanov et al. (1990) considered Unit III as a normal continuous sedimentary succession and the upward decrease in metamorphism, from greenschist facies to anchimetamorphic, as a gradual temperature decrease in a regional metamorphic setting.

Unit IV

The uppermost unit of the study area is formed by tectonic klippen of leucocratic, muscovite-rich orthogneiss, resting along a subhorizontal, gently folded contact either on Unit III or where the latter is absent, on Unit II (Fig. 2). Subordinate rock types occurring in this unit are amphibolite and marble. In contrast to the underlying Unit II, the gneiss of Unit IV is only little chloritised, so that its whitish colour contrasts with the dark green to brown colour of the underlying rocks. Bonev et al. (2010a) determined ^{39}Ar–^{40}Ar muscovite ages of ca. 154 Ma and ca. 157 Ma on two samples from Unit IV, indicating cooling below ca. 350 °C already in the Jurassic. These are so far the only geochronological data from the metamorphic rocks of the study area.

The metamorphic units II, III, and IV are unconformably overlain by Upper Eocene sediments (Fig. 2) of the Podrumche Formation (Sarov et al. 2008), unsorted clastic sediments with grain sizes varying between sand and more than 5 metres large blocks. The components are metamorphic rocks, partly the same types as occur in the tectonic units of the study area. They are rounded to variable degrees. The colour is red-brown to grey. The absence of any sorting suggests deposition by debris flows from nearby, steep slopes. The unconsolidated nature of the sediments shows that they were not deeply buried but remained close to the surface since their deposition. To the east, the sediments are overlain by volcanoclastic and volcanic rocks of the ca. 32.7–32.2 Ma old Madjarovo volcanic complex (Marchev and Singer 2002).

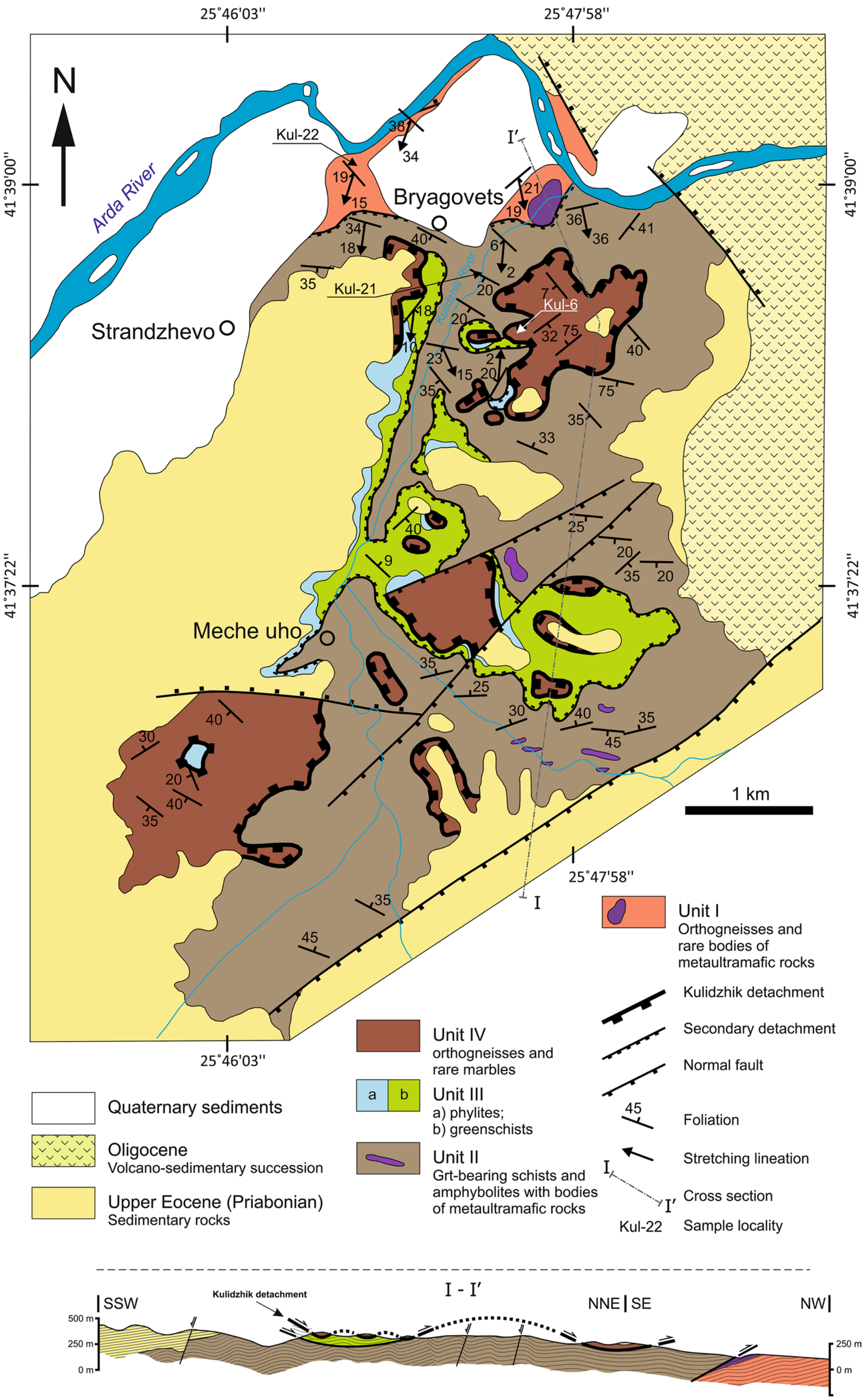

Fig. 2 Geological map and cross section of the study area, modified after Boyanov (1969), Bonev (2006a) and Sarov et al. (2008)

Previous tectonic interpretations

The south- to southwest-directed tectonic transport recorded in the high-grade basement of the Bulgarian Rhodopes is mostly interpreted as related to Cretaceous compressional tectonics (Ivanov 1989; Burg et al. 1996; Ivanov 1998; Burg 2012; Dimov et al. 2000; Bonev 2006a, b; Bonev et al. 2006a, b), whereas the north- or south-directed lower-grade

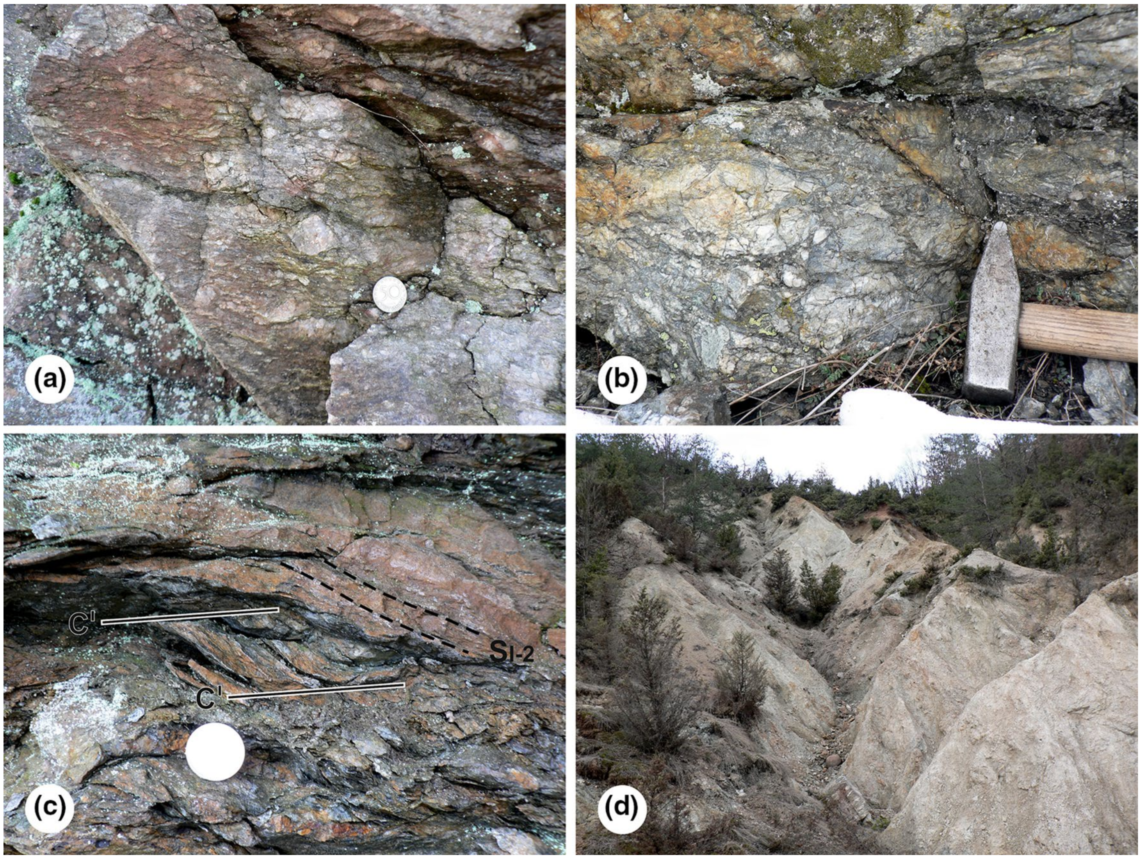

Fig. 3 Field photographs of deformation structures in the study area. **a** Augengneiss of Unit I, at the sampling locality of Kul-22 on the road from Strandzhevo to Bryagovets. Diameter of coin is 23 mm. **b** Cohesive, chlorite-rich cataclastic breccia at the top of Unit II. Eastern slope of Kulidzhik valley, 1 km south of Bryagovets. **c** Ductile to brittle shear structure overprinting the augengneiss of Unit I. S-C' structure with sigmoidally deformed foliation indicates sinistral, i.e. top-to-the north displacement. Arda river bank north of Bryagovets. Diameter of coin is 23 mm, north is to the left. **d** Badland erosion in light-coloured, cohesionless kakirite formed from muscovite gneiss at the base of Unit IV, Kulidzhik valley 0.8 km east of Meche uho

mylonitization that has affected different parts of the Rhodope basement is viewed as an effect of postorogenic extensional collapse and formation of asymmetric metamorphic core complexes in the Tertiary (Ivanov 1989, 1998; Dimov et al. 2000; Burg et al. 1996; Bonev 2006a; Bonev et al. 2006b). This traditional view has been challenged by Gerdjikov and Gautier (2005), Gerdjikov et al. (2010), Bosse et al. (2009) and Gautier et al. (2010) and later by Jahn-Awe et al. (2010) and Kirchenbaur et al. (2012), based on zircon dating and Lu–Hf eclogite dating, respectively. These authors argued that the underthrusting of the Lower Allochthon, with a top-south to -southwest shear sense, is Paleogene in age. On the other hand, the top-north tectonic transport recorded within the uppermost tectonic units of the Eastern Rhodope area (Uppermost Allochthon) has been interpreted to reflect the Late Jurassic—Early Cretaceous collision and northward obduction of a Jurassic volcanic arc onto the high-grade basement units of the Rhodope Metamorphic Complex (Bonev et al. 2010a).

With respect to the Kulidzhik area, only few tectonic interpretations have been published (Boyanov 1969; Boyanov et al. 1969, 1990; Bonev 2006a; Bonev et al. 2010a; Sarov et al. 2008). The map of Boyanov (1969) distinguished an autochthonous crystalline basement (including our Units I and II), the "Diabaso-phyllitoid Formation", interpreted as the Late Proterozoic to Early Paleozoic cover of the basement (our Unit III), and the allochthonous "Proterozoic metamorphic rocks of the Allochthon" (our Unit IV). Boyanov et al. (1969) interpreted Unit II as former high-grade basement, transformed into phyllonite by shearing and retrograde metamorphism. Later maps (Bonev 2006a; Bonev et al. 2010a; our Fig. 2) are still mainly based on this detailed map. Boyanov (1969) assumed pre-Paleogene thrust emplacement of Unit IV towards east-northeast along a subhorizontal surface. After the finding of fossils in Unit III, first determined as Early Cretaceous (Boyanov and Lipman 1973) but then interpreted as Early Jurassic (Tikhomirova et al. 1988), Boyanov et al. (1990)

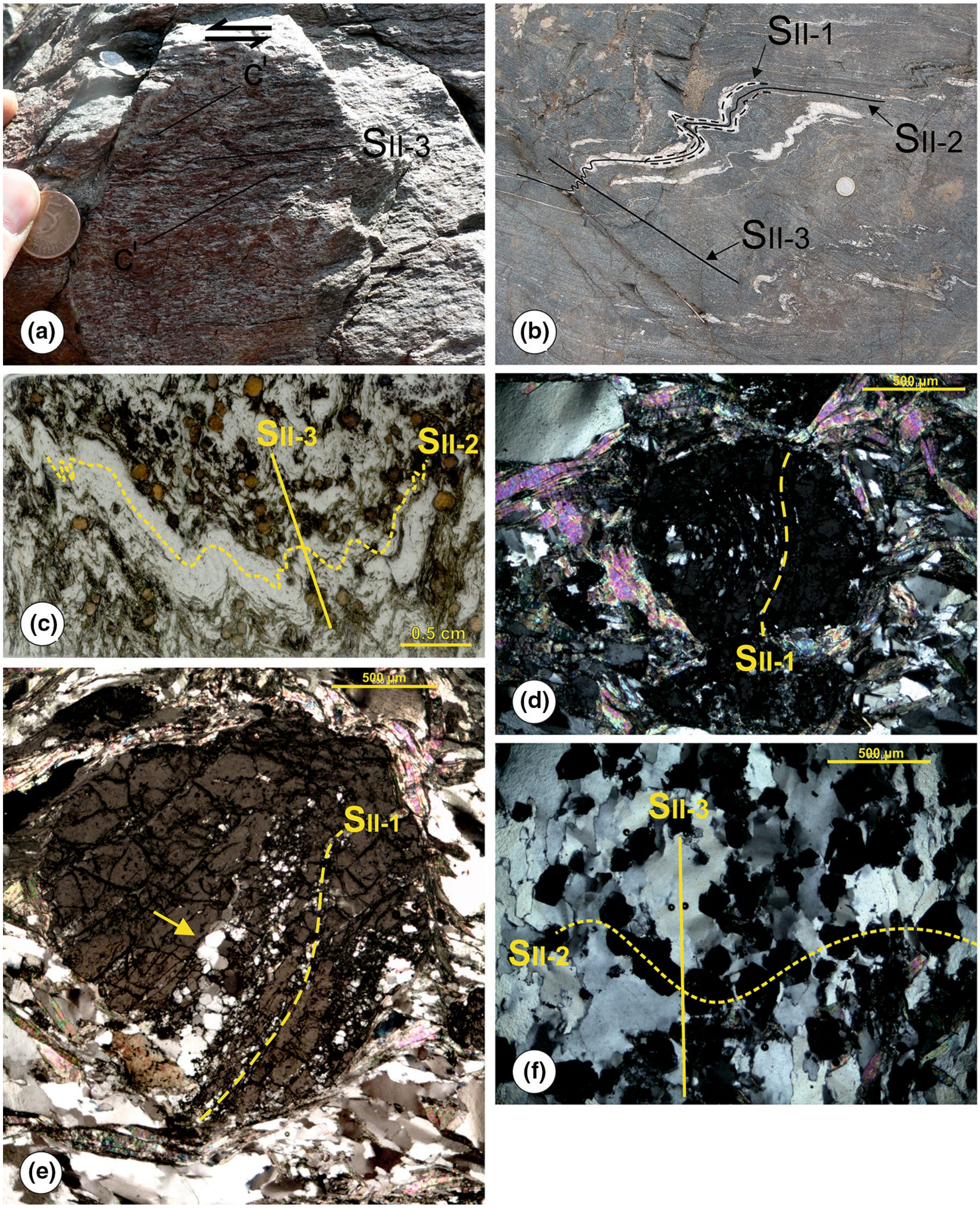

Fig. 4 Outcrop and thin-section photographs of (**a**) mylonitic garnet-bearing schist from the uppermost section of Unit II exhibiting a clear S-C' pattern and consistent top-to-the north sense of shear (outcrop at the eastern end of Bryagovets village, coordinates: 41°38′51.95″N/25°47′39.24″E); **b**–**f** garnet-bearing schist in Unit II, at the sampling locality of Kul-21. **b** Relationships between S_{II-1} S_{II-2} and S_{II-3}. S_{II-3} are developed as an axial cleavage of centimetre scale open folds formed by S_{II-2}. Note the trace of the S_{II-2} foliation which also acted as an axial plane of older generation isoclinal folds formed by S_{II-1} (*dashed line*). The latter being underlined by different in colour and composition "layers". **c** A polished hand specimen of the same garnet-bearing schist, showing relationships between S_{II-2} and S_{II-3}. S_{II-3} is developed as an axial cleavage of centimetre to millimetre scale folds of S_{II-2}. **d** Cracked and partly resorbed garnet from the first generation. The inclusions within the former garnet porphyroblast form an older foliation (S_{II-1}) that is at a high angle with respect to the later main fabric of the rock. **e** A similar partly resorbed garnet porphyroblast from the first generation that exhibits a clear s-shaped older (S_{II-1}) foliation formed by different (mainly quartz) inclusions and an elongated zone (centre to bottom of the garnet) filled with polygonal quartz (the *yellow arrow* pointing the upper tip of that elongated zone). **f** A microphotograph showing the relationships between S_{II-2} and S_{II-3}. S_{II-2} is underlined by the second generation of small and euhedral garnet porphyroblasts that form millimetre scale open folds. S_{II-3} developed parallel to the axial plane of those folds and is underlined mostly by elongated and dynamically recrystallised quartz grains

suggested that the thrusting of the Kulidzhik Nappe took place in the "Austrian Phase" (Late Aptian).

Bonev (2006a) collectively correlated the high-grade metamorphic rocks that comprise our units I and II to the upper high-grade basement of the Eastern Rhodopes, i.e. the Upper Allochthon. On the geological map of Bulgaria M 1:50,000 (Sarov et al. 2008) Unit I is assigned to the Krumovitsa Lithotectonic unit (Upper Allochthon) and units II, III, and IV to the Mandritsa Lithotectonic Unit (Uppermost Allochthon). Bonev et al. (2010a) correlated Unit I with the gneisses exposed in the core of Byala Reka-Kechros Dome south of the study area, i.e. the Lower Allochthon. They merged the retrogressed high-grade rocks from the Kulidzhik area (our Unit II) together with the overlying low-grade rocks (our Unit III) and assigned both to the Mesozoic low-grade unit, i.e. the Uppermost Allochthon. Bonev (2006a) suggested that the high-grade rocks of the Kulidzhik Nappe (Unit IV) were emplaced on Unit III by amphibolite-facies shearing in a synmetamorphic, top-southwest thrust of Cretaceous age. When the Jurassic cooling ages in Unit IV were determined, Bonev et al. (2010a) changed the interpretation of the basal contact of Unit IV into a top-north-northeast thrust, active during a Jurassic-age arc-continent collision. These authors also assumed that Unit IV is indistinguishable from the lower high-grade basement of the Eastern Rhodopes (Lower Allochthon), "thus representing an extension of this unit in the study area", although it is not at the base but at the top of the tectonic pile. Most workers interpreted the nature of the contact between units III and IV in terms of shortening and thrusting. Only Bonev et al. (2010a) mentioned the importance of Tertiary extensional tectonics.

Results

Structural observations

Unit I

Unit I crops out along the Arda River in the northern part of the study area (Fig. 2). The orthogneisses are partly equigranular, partly typical augen gneisses (Fig. 3a) and generally represent S-L tectonites. Unit I was affected by two shearing deformation events with opposite kinematics, an older, penetrative one (top-south) and a younger, more localised one (top-north).The older foliation, $S_{I\text{-}1}$, is pervasive in the entire outcrop area except at the top of the unit where the younger fabric prevails. $S_{I\text{-}1}$ is defined by quartz domains (ribbons), lens-shaped K-feldspar porphyroclasts (in the case of augengneiss), and layers rich in muscovite and partly chloritised biotite. $S_{I\text{-}1}$ dips southeast to southwest at low to moderate angles (Fig. 5a). It bears a pronounced stretching lineation ($L_{I\text{-}1}$). This stretching lineation is defined by elongate quartz aggregates, lenticular feldspar porphyroclasts and elongate aggregates of muscovite and biotite grains. Towards the structural top of Unit I, biotite is more and more chloritised. The $L_{I\text{-}1}$ lineation plunges south to southwest (Fig. 5a). Shear bands and asymmetric K-feldspar porphyroclasts consistently indicate top-south to top-southwest-directed mylonitic shearing. Under the microscope, this shear sense is confirmed by mica fishes (Fig. 6a), oblique grain shape of recrystallised quartz (Fig. 6b), and small shear bands (Fig. 6c). Quartz shows recrystallization by subgrain rotation (Fig. 6b) which suggests greenschist facies conditions (ca. 400–500 °C) during deformation (Stipp et al. 2002). Dynamically recrystallised feldspar, observed in porphyroclast tails and as mantle around porphyroclasts, indicates temperatures in the same range or higher. Some samples show quartz recrystallization by grain-boundary migration, indicating temperatures above ca. 500 °C during deformation. However, a subsequent formation of smaller quartz grains by the subgrain rotation mechanism (Fig. 6a, b) shows that top-south-southwest shearing went on under decreasing temperatures.

This fabric is overprinted by north-dipping, subhorizontal or south-dipping, ductile to brittle shear zones which locally formed a second foliation $S_{I\text{-}2}$ and C'-type shear bands that cut $S_{I\text{-}2}$ at moderate angles (Fig. 3c). Often $S_{I\text{-}1}$ is dragged into parallelism with $S_{I\text{-}2}$. Fine-grained white mica and chlorite are found along the $S_{I\text{-}2}$ foliation planes. $S_{I\text{-}2}$ bears a new stretching lineation, $L_{I\text{-}2}$, defined by aggregates of fine-grained white mica and chlorite and quartz slickenfibres. $L_{I\text{-}2}$ plunges shallowly north to north-northwest or south to south-southeast (Fig. 5b). Flat or gently north-dipping shear bands and progressive reorientation of the older foliation, i.e. drag, indicate top-north to -north-northwest shearing during this second deformation phase (Fig. 3c).

As a rule, the $S_{I\text{-}2}$ foliation is more penetratively developed towards the contact with Unit II. At the contact itself, the $S_{I\text{-}2}$ fabric is predominant. Locally, at some distance from the contact, two competing stretching lineations $L_{I\text{-}1}$ and $L_{I\text{-}2}$ were observed on the same foliation surface, $L_{I\text{-}1}$ trending more northeasterly and $L_{I\text{-}2}$ more northwesterly. The complete chloritization of biotite in shear zones with a strong $S_{I\text{-}2}/L_{I\text{-}2}$ fabric indicates that this second deformation phase took place under conditions of the lower greenschist facies.

Unit II

Unit II consists of high-grade metamorphic rocks that were affected by mylonitization under greenschist facies conditions. These produced the main foliation ($S_{II\text{-}3}$). $S_{II\text{-}3}$ is the only penetrative foliation in the intensely sheared upper

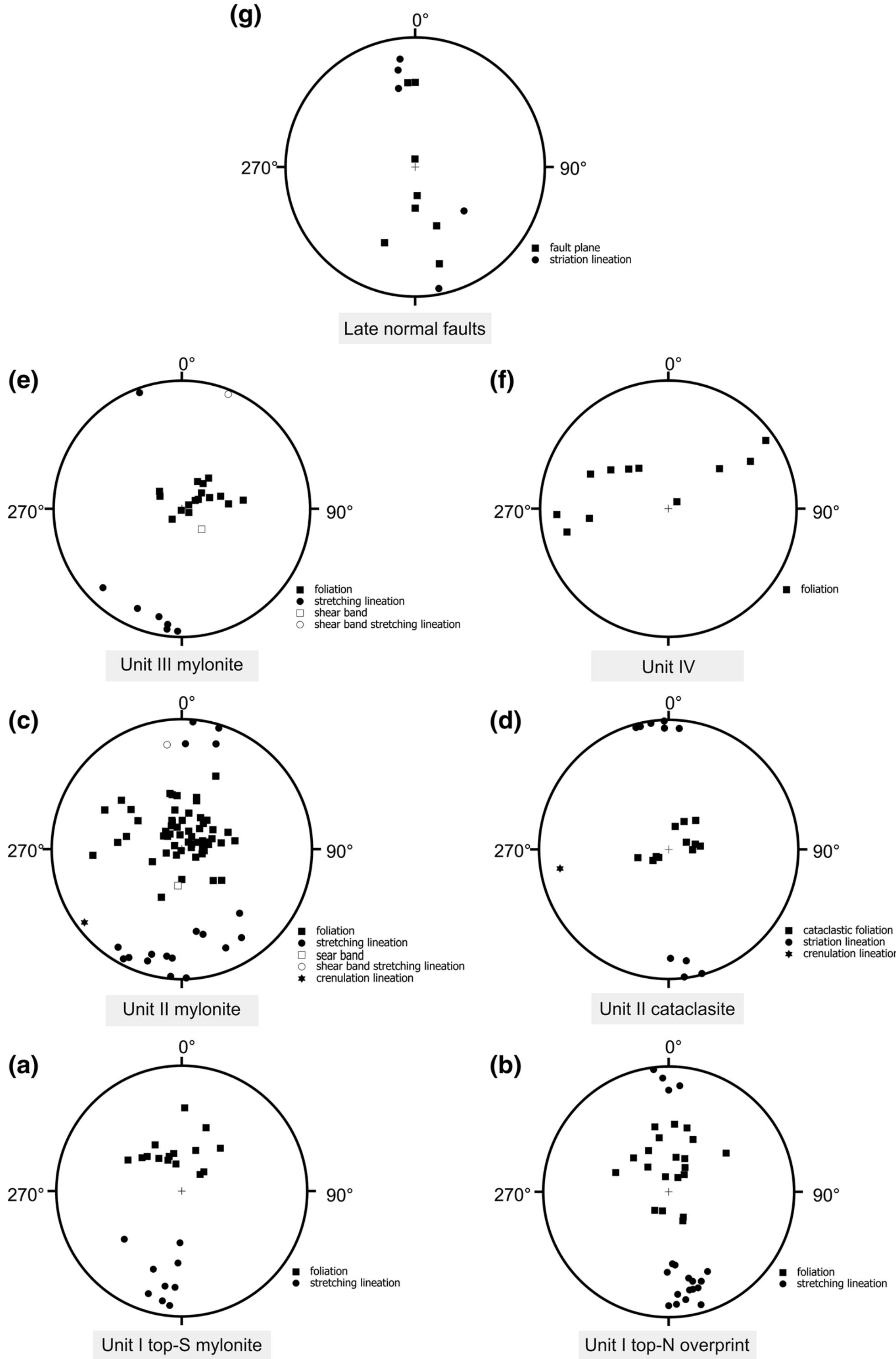

Fig. 5 Schmidt nets representing the orientations of structural elements in the study area (equal area projection, lower hemisphere, N is up). **a** Foliation $S_{I\text{-}1}$ and stretching lineation $L_{I\text{-}1}$ from Unit I. **b** Foliation $S_{I\text{-}2}$ and stretching lineation $L_{I\text{-}2}$ from Unit I. **c** Foliation $S_{II\text{-}3}$ and stretching lineation $L_{II\text{-}3}$ from Unit II. **d** Structural elements of cataclasite from Unit II. **e** Structural elements of Unit III. **f** Secondary rank fault surfaces and related slickensides and slickenfibres within the ultracataclastic domain of the Kulidzhik Detachment Fault. **g** Foliation in Unit IV. **h** Orientation of late normal fault planes and striations

part of Unit II, close to the contact with the overlying Unit III (Fig. 4a). In the lower part, $S_{II\text{-}3}$ is less strongly developed and metapelitic schists have preserved two older foliations from an earlier metamorphic event (Fig. 4). There, $S_{II\text{-}3}$ is the axial planar foliation of open folds deforming an older foliation, $S_{II\text{-}2}$ (Fig. 4b, c, f). This older foliation is itself axial planar with respect to isoclinal folds which deform a still older planar fabric ($S_{II\text{-}1}$) marked by the alternation of dark, mica-rich and light, quartz-rich layers (Fig. 4b).

Two generations of garnet are present in the schists from Unit II. The older garnets are larger (up to several

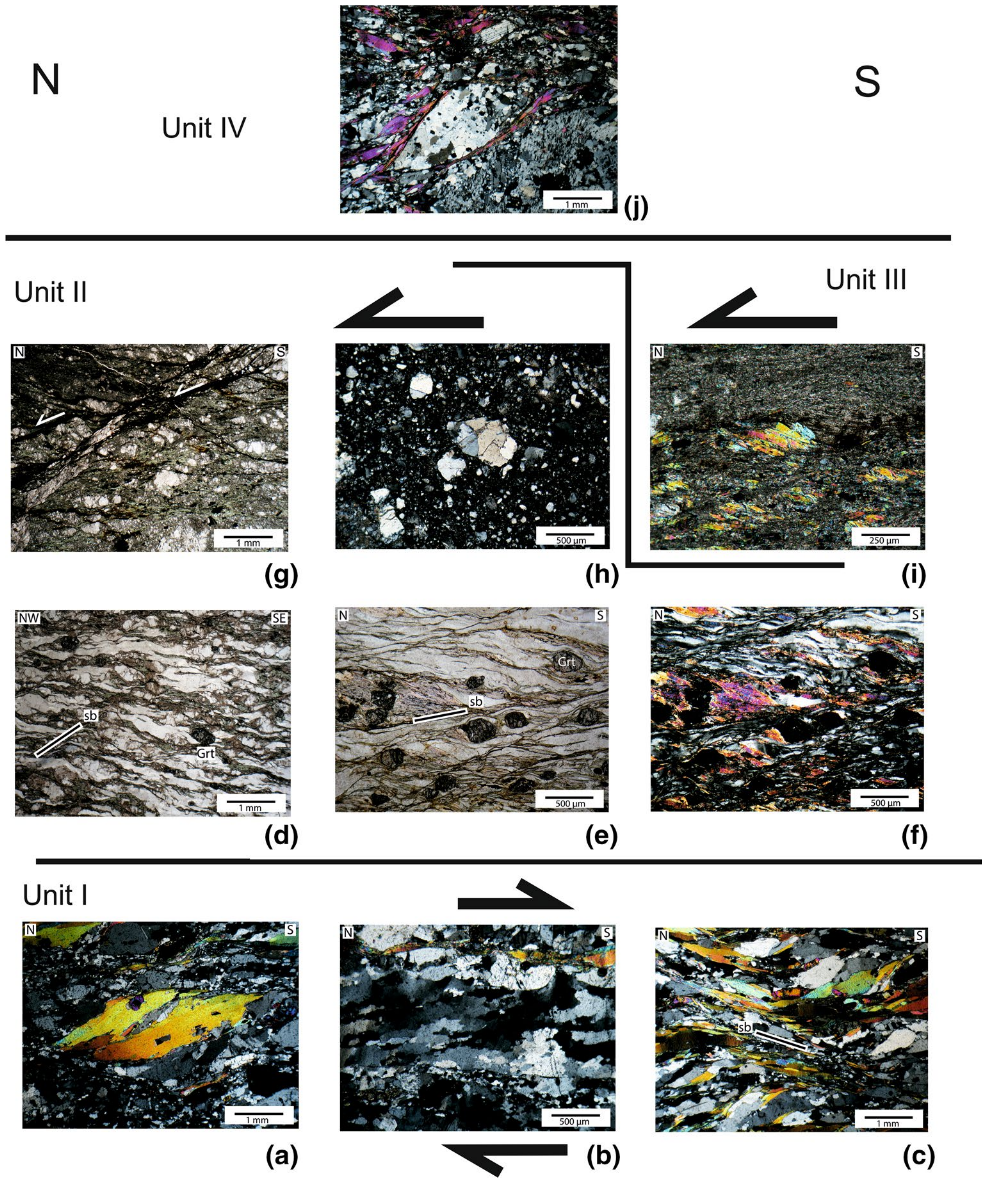

Fig. 6 Thin-section photographs of deformation structures in the study area: **a** Muscovite mica fishes within the augengneiss from Unit I. The asymmetry of the muscovite clast shows dextral (top-to-the southwest) sense of shear. **b** A shape preferred orientation of dynamically recrystallised subgrains in quartz oblique to the main S_{I-1} foliation of the orthogneisses from Unit I. The oblique position of the subgrains points to the top-to-the southwest shearing in upper greenschist facies conditions (ca. 400–500 °C). **c** A microphotograph of a sheared orthogneiss from Unit I with dipping to the right (southwest) shear bands underlined by newly formed white mica and small grained quartz and feldspar clasts. The small angle between the main foliation and the shear band points to a top-to-the southwest sense of shear. **d**–**f** Top-to-the north greenschist facies mylonites from the upper structural section of Unit II, note the garnet is still preserved and forms clear asymmetric sigma-shaped clasts. **g** Foliated cataclasite with dipping to the north, synthetic to the main cataclastic foliation Riedel failures that indicate top-to-the north sense of shear. **h** Cohesive cataclasite of the detachment fault zone located between units II and III. **i** Mylonites of Unit III containing asymmetric mica fishes (muscovite) that indicate top-to-the north sense of shear in the entire outcrop area of the unit. **j** A protomylonite fabric of the orthogneiss from Unit IV (the klippen). Note the ductile deformation of the K-feldspar which dynamic recrystallization points to a higher grade (at least high-greenschist to lower amphibolite facies conditions)

millimetres), strongly resorbed and fractured, and contain inclusions of quartz, biotite, muscovite, plagioclase and rutile (Fig. 4d, e). The inclusions form an internal foliation oriented at high angle to the external foliation S_{II-2}. We tentatively correlate this internal foliation with S_{II-1}. In some first-generation garnet grains, larger inclusions are filled with polycrystalline quartz showing polygonal grain boundaries (Fig. 4e). Such polycrystalline, polygonal quartz is not found outside these garnet grains and points either to static recrystallization at elevated temperatures or to recovery after the transformation of coesite to quartz (Wain et al. 2000). The latter would be a first, albeit weak hint to correlate Unit II with the ultrahigh-pressure Krumovitsa-Kimi unit of the Upper Allochthon, a correlation strongly supported by our zircon dating (see below).

The garnet porphyroblasts of the second generation are smaller (ca. 200 μ) and euhedral. In some places, they trace the S_{II-2} foliation (Fig. 4f). At outcrop-scale and under the microscope, S_{II-2} is intensely folded. The axial planar cleavage of these folds, S_{II-3}, is defined by reoriented older mica flakes, newly grown white mica and chlorite, and the grain shape of dynamically recrystallised quartz (Fig. 4f). The recrystallization mechanism in quartz is low-temperature bulging which, together with the abundance of deformation bands and undulose extinction in quartz as well as the growth of chlorite, suggests temperatures of 300–400 °C (Stipp et al. 2002) during the deformation process that resulted in S_{II-3} formation.

Towards higher structural levels within Unit II, the S_{II-3} foliation becomes more pronounced and attains a subhorizontal to shallowly dipping orientation (Fig. 5c). The rock is progressively transformed into a mylonite, and older deformation structures become indistinguishable. The foliation bears a stretching lineation plunging shallowly south or north (Fig. 5c). In schists the lineation is defined by aligned white mica and chlorite flakes, stretched quartz ribbons, and pressure shadows of garnet crystals, whereas in amphibolites it is defined by elongated needles of dark amphibole, partly retrogressed to actinolite, and replaced by epidote and chlorite.

Viewed in surfaces perpendicular to the foliation and parallel to the lineation, the mylonites exhibit a consistent top-north shear sense, documented by abundant shear bands, mica fishes, and asymmetric garnet porphyroclasts (Fig. 6d–f).

Since the rocks were originally rich in biotite, garnet, and amphibole, mylonitization under lower greenschist facies conditions turned them into chlorite-rich phyllonites and retrograde greenschists. However, lower-strain domains with strongly chloritised garnet can still be observed also in structurally higher parts of Unit II. The contact zone with the overlying Unit III represents an up to several metres thick, flat-lying layer of partly foliated cataclasites (Figs. 3b, 6g, h). The cataclastic foliation is roughly parallel to the contact and bears a slickenside lineation plunging shallowly north or south (Fig. 5d). Where the shear sense of the cataclasites can be determined from slicken fibre steps, synthetic Riedel shears (Fig. 6g), and drag, it is consistently top-north. The progressive mylonitization and subsequent cataclasis recorded in the rocks of Unit II point to a gradual temperature decrease and to the extensional nature of the contact with the overlying Unit III.

Unit III

The rocks of Unit III are greenschists, phyllites, and calcschists. It is not easy to distinguish the first two rock types from the phyllonites and retro-greenschists of Unit II, which is probably the reason why Sarov et al. (2008) and later Bonev et al. (2010a) made no distinction between the two units. On the map of Boyanov (1969), however, the boundary is mapped and our own observations confirmed its location. Our field observations also confirmed that the metamorphic grade in Unit III decreases up-section, whereas greenschist facies rocks (greenschists and phyllites) prevail, unmetamorphic or anchizonal slate and siltstone locally occur at the top of Unit III.

The rocks have a moderately dipping foliation and locally a N–S- to NE–SW-oriented stretching lineation (Fig. 5e). The stretching lineation is best developed in the calcschists, probably because calcite is most easily dynamically recrystallised at low temperatures. The sense of shear as indicated by shear bands at outcrop scale and mica fish and shear bands at microscopic scale (Fig. 6i) is top-north. The ductile fabric is in many places overprinted by brittle deformation, which prevails within the upper structural levels of Unit III close to the contact with Unit IV. The contact represents an up to several metres thick layer of brittle fault rocks (Fig. 3b) represented by non-cohesive breccia (kakirite). The kakirite represents the lowermost and tectonically crushed rocks of Unit IV. Despite the lack of kinematic indicators, due to the similar style, we assume that the shearing deformation belongs to the same (extensional) process as the one that formed the mylonites and cataclasites in Unit II. Extensional shearing may also explain the above-mentioned upward transition from greenschist facies to anchizonal on a very small vertical distance of only a few tens of metres.

Unit IV

The muscovite gneisses of Unit IV are rather similar to augengneisses of Unit I but are distinguished by the frequent occurrence of up to cm large muscovite flakes. In thin section, these are set between partly dynamically recrystallised, perthitic, augen-shaped K-feldspar porphyroclasts, forming a protomylonitic fabric (Fig. 6j). The dynamic recrystallization of feldspar suggests amphibolite-facies or at least upper greenschist facies conditions for the deformation. The gneiss foliation is variably oriented, partly steep, and folded. The measurements suggest a north–south oriented fold axis (Fig. 5f). The foliation is often oriented at a high angle to the basal contact of the unit. It is overprinted by wide-spread and pervasive brittle deformation, particularly intense along the base. In many places the gneiss is transformed into a non-cohesive tectonic breccia, i.e. a kakirite, of cm-sized fragments. These rocks form badlands reminiscent of those in non-cohesive sediments (Fig. 3d). Even where the rocks are strongly shattered, the fragments look rather fresh under the microscope and chloritization is only weak or absent. This contrasts strongly with the pervasive alteration and chloritization in Unit II. Therefore, it appears that the brittle deformation of Unit IV took place at a shallow level near the Earth's surface. It is clear that the protomylonitic structure of the gneisses is unrelated to the basal fault horizon along which Unit IV now rests on the deeper units.

The entire metamorphic pile as well as the Eocene sediments is cut by brittle, mostly north-dipping, normal faults (Figs. 2, 5g).

Geochronology

Sample description

Sample Kul-22 is a mylonitic augengneiss from Unit I. It was collected along the road between the villages Bryagovets and Strandzhevo (sample coordinates: 41°39′05.7″N/25°46′48.0″E, see also Fig. 2). This sample is composed of perthitic potassium feldspar forming up to cm-sized augen, plagioclase, quartz, white mica, chlorite after biotite, opaque phases and accessory zircon.

Sample Kul-21 is a garnet-chlorite-mica-schist from Unit II. It was collected at an outcrop in the Kulidzhik River bed (sample coordinates: 41°38′37.10″N/25°47′25.82″E, see also Fig. 2). The sample comprises: major quartz (>50 %vol, garnet, white mica, biotite, plagioclase and chlorite; minor tourmaline and opaque mineral; and accessory rutile, epidote, apatite and zircon. Three principal mineral assemblages, which indicate different stages of the metamorphic evolution, have been distinguished in this sample. The earliest assemblage is composed of garnet porphyroblasts (2–4 mm size) and inclusions of quartz, biotite, white mica, plagioclase and rutile within garnet. The porphyroblasts are rotated, fractured, and strongly resorbed (Fig. 4c, d). Their formation predates the penetrative foliation of the sample. The second assemblage forms the foliation $S_{II\text{-}2}$. It includes small euhedral garnet (≤ 1 mm) and tourmaline (<0.5 mm) in a matrix of abundant quartz and white mica, minor biotite and plagioclase. The third assemblage corresponds to the foliation $S_{II\text{-}3}$ and represents lower greenschist facies retrogression with chlorite replacing garnet and biotite, accompanied by white mica, sagenite rutile in chlorite and in white mica, opaque Fe-oxide phase around resorbed garnets, epidote, and quartz. Brittle fractures filled with chlorite and minor carbonate mark a final stage of retrogression.

Sample Kul-6 is a protomylonitic muscovite gneiss from Unit IV. It was collected on the large klippe southeast of Bryagovets village (sample coordinates: 41°38′23.82″N/25°47′53.58″E, see also Fig. 2). The rock is composed of perthitic K-feldspar forming augen and partly dynamically recrystallised, plagioclase, quartz, large (up to cm) muscovite flakes, little chlorite, zircon and opaque phases.

Analytical methods and sample preparation

The samples were studied using: LA-ICPMS for U–Pb zircon dating and trace elements contents in dated zircon grains, EMP for chemical composition of mineral inclusions in zircon, and XRF for whole-rock chemistry. Details for sample preparation and analytical procedures are provided in Appendix A (ESM), operational parameters of instruments used for LA-ICP-MS dating in Appendix B (ESM). The results of zircon dating are presented in Tables 1, 2 and 3. Geochemical data are provided in Appendices, namely: Appendix C (ESM) for REE and other trace elements contents (ppm) in dated zircons; Appendix D (ESM) for contents of major oxides (wt%) and trace elements (ppm) in whole-rock samples; and Appendix E (ESM) for chemical composition (major oxides, wt%) of mineral inclusions in zircon grains.

Results

Kul-22 (K-feldspar augengneiss from Unit I)

The zircon separate from the augengneiss contains colourless to pale beige and transparent to translucent euhedral grains of uniform prismatic morphology with length/width ratios ≥2 commonly. The CL images display fine oscillatory zoning, frequently obscured and homogenised with decreasing CL intensity towards crystal rims (Fig. 7a). Few grains contain xenocrystic (image 11) or antecrystic cores of unzoned, patchy or chaotic textures. Some cores are CL dark (metamict, image 23) with radial fissures in the surrounding oscillatory zoned domains. Inclusions of quartz, K-feldspar, muscovite and apatite were found both in antecrystic and oscillatory zoned domains.

The zircon ages vary between 278 and 334 Ma except for one xenocrystic core that is 567 Ma old (Table 1). Similar age variation was found for cores (334–287 Ma), oscillatory zoned domains (315–289 Ma) and rims (318–278 Ma). Most of the data are concordant, scattering along the concordia and clustering around 300 Ma on the probability density diagram (Fig. 7b). The weighted mean $^{206}Pb/^{208}U$ age is 300.7 ± 2.6 Ma, excluding the youngest and the oldest zircons (Isoplot outlier rejection via a modified 2-sigma set of criteria). Seven results that overlap within 2σ age error yield a concordia age of 301.9 ± 2.4 Ma (Fig. 7c).

Table 1 U–Pb isotopic composition and dating of zircons from sample Kul 22 (*c* core, *o* oscillatory domain, *dr* dark rim)

Zircon analysis	Th (ppm)	U (ppm)	Pb (ppm)	Th/U	Isotope ratio for Whederill plot[a,b]				Rho[c]	Isotope ratios[a,b]				Age estimates (Ma)				Concordance[d]
					$^{207}Pb/^{235}U$	1σ	$^{206}Pb/^{238}U$	1σ		$^{208}Pb/^{232}Th$	1σ	$^{207}Pb/^{206}Pb$	1σ	$^{206}Pb/^{238}U$	2σ	$^{207}Pb/^{235}U$	2σ	
1c	146	209	11.1	0.70	0.34191	0.02094	0.04874	0.00078	0.55	0.0143	0.0007	0.0509	0.0032	306.86	9.59	298.66	31.36	103
1dr	79	254	12.4	0.31	0.54694	0.02470	0.04645	0.00074	0.57	0.0201	0.0011	0.0854	0.0040	292.79	9.11	443.04	32.03	66
2c	59	79	4.2	0.74	0.36866	0.03354	0.04853	0.00097	0.55	0.0137	0.0008	0.0551	0.0051	305.57	11.92	318.71	48.95	96
2r	47	66	3.5	0.72	0.34932	0.04338	0.04917	0.00107	0.54	0.0139	0.0009	0.0515	0.0065	309.50	13.14	304.26	63.91	102
3c	443	265	17.0	1.67	0.35837	0.01614	0.04845	0.00068	0.56	0.0135	0.0007	0.0537	0.0025	305.04	8.36	311.04	23.94	98
3dr[e]	274	312	16.6	0.88	0.32751	0.01503	0.04794	0.00067	0.56	0.0129	0.0007	0.0496	0.0023	301.93	8.24	287.71	22.82	105
5c	292	251	13.8	1.16	0.34107	0.01820	0.04550	0.00068	0.56	0.0132	0.0008	0.0544	0.0030	286.90	8.38	298.03	27.31	96
5o	217	352	17.7	0.62	0.35068	0.01377	0.04727	0.00064	0.57	0.0136	0.0009	0.0538	0.0022	297.82	7.88	305.28	20.56	98
5dr	311	979	49.1	0.32	0.38093	0.01162	0.05059	0.00063	0.58	0.0152	0.0010	0.0546	0.0017	318.24	7.73	327.77	16.99	97
6c	56	63	3.4	0.89	0.35344	0.04699	0.04717	0.00106	0.54	0.0147	0.0010	0.0544	0.0073	297.20	13.04	307.35	68.90	97
8c	255	244	13.8	1.04	0.36699	0.01673	0.04842	0.00069	0.56	0.0136	0.0009	0.0550	0.0026	304.88	8.48	317.47	24.65	96
8dr	416	1481	70.2	0.28	0.34364	0.00962	0.04875	0.00058	0.58	0.0133	0.0009	0.0511	0.0015	306.94	7.13	299.97	14.47	102
9c	134	157	8.2	0.85	0.32614	0.02643	0.04595	0.00085	0.55	0.0141	0.0011	0.0515	0.0042	289.68	10.47	286.66	39.95	101
9dr	298	1142	53.9	0.26	0.34933	0.01074	0.04872	0.00060	0.58	0.0137	0.0011	0.0520	0.0017	306.76	7.37	304.26	16.08	101
11c	40	54	10.1	0.74	5.38420	0.19851	0.09195	0.00223	0.59	0.1098	0.0061	0.4247	0.0178	567.14	26.30	1 882.39	57.60	30
11o	427	357	19.8	1.20	0.34531	0.01403	0.04579	0.00062	0.57	0.0130	0.0007	0.0547	0.0023	288.68	7.64	301.23	21.03	96
14c	68	121	6.3	0.56	0.32560	0.02767	0.04876	0.00085	0.54	0.0157	0.0010	0.0484	0.0042	306.99	10.44	286.25	41.81	107
14dr	169	718	32.0	0.24	0.34099	0.01007	0.04613	0.00056	0.58	0.0133	0.0008	0.0536	0.0016	290.82	6.90	297.97	15.17	98
15c	471	769	42.8	0.61	0.43543	0.01275	0.05320	0.00065	0.58	0.0132	0.0008	0.0594	0.0018	334.22	7.95	367.07	17.92	91
15o	345	277	15.8	1.25	0.32703	0.01653	0.04685	0.00068	0.56	0.0132	0.0008	0.0506	0.0026	295.21	8.37	287.34	25.09	103
16c	212	473	23.6	0.45	0.35836	0.01402	0.04941	0.00067	0.57	0.0133	0.0010	0.0526	0.0021	310.99	8.23	311.04	20.81	100
16r	86	448	19.8	0.19	0.34492	0.01348	0.04634	0.00063	0.57	0.0133	0.0010	0.0540	0.0022	292.11	7.76	300.94	20.22	97
17c	167	330	16.8	0.50	0.39374	0.01606	0.04917	0.00068	0.57	0.0135	0.0009	0.0581	0.0024	309.51	8.35	337.14	23.21	92
17dr	228	1225	51.3	0.19	0.31448	0.00934	0.04403	0.00054	0.58	0.0126	0.0009	0.0518	0.0016	277.87	6.67	277.69	14.36	100
18c	398	455	24.0	0.87	0.32572	0.01282	0.04706	0.00062	0.57	0.0131	0.0008	0.0502	0.0020	296.52	7.63	286.34	19.51	104
19o[e]	255	310	16.2	0.82	0.33256	0.01647	0.04780	0.00070	0.56	0.0126	0.0010	0.0505	0.0025	301.08	8.61	291.57	24.89	103
22dr	355	1066	19.4	0.33	0.34513	0.01078	0.04716	0.00059	0.58	0.0123	0.0009	0.0531	0.0017	297.16	7.26	301.10	16.19	99
22o	281	976	46.4	0.29	0.36842	0.01222	0.04872	0.00063	0.58	0.0132	0.0010	0.0549	0.0018	306.76	7.74	318.53	18.02	96
23o	350	1216	59.2	0.29	0.36588	0.00933	0.05016	0.00058	0.59	0.0130	0.0007	0.0529	0.0014	315.60	7.12	316.64	13.81	100
26c[e]	212	195	10.8	1.09	0.34390	0.01992	0.04770	0.00073	0.55	0.0127	0.0007	0.0523	0.0031	300.45	8.98	300.17	29.80	100
30o	126	468	21.2	0.27	0.34609	0.01189	0.04658	0.00059	0.57	0.0133	0.0009	0.0539	0.0019	293.59	7.27	301.82	17.83	97
31o	292	412	21.3	0.71	0.35362	0.01389	0.04841	0.00064	0.57	0.0126	0.0008	0.0530	0.0021	304.83	7.87	307.49	20.69	99
33c	107	497	22.9	0.22	0.33715	0.01411	0.04817	0.00066	0.57	0.0138	0.0010	0.0508	0.0022	303.38	8.12	295.06	21.28	103
34c[e]	176	318	15.9	0.55	0.36670	0.01591	0.04801	0.00067	0.56	0.0131	0.0010	0.0554	0.0025	302.38	8.24	317.25	23.45	95

Table 1 continued

Zircon analysis	Th (ppm)	U (ppm)	Pb (ppm)	Th/U	Isotope ratio for Whederill plot[a,b]				Rho[c]	Isotope ratios[a,b]				Age estimates (Ma)				Concordance[d]
					$^{207}Pb/^{235}U$	1σ	$^{206}Pb/^{238}U$	1σ		$^{208}Pb/^{232}Th$	1σ	$^{207}Pb/^{206}Pb$	1σ	$^{206}Pb/^{238}U$	2σ	$^{207}Pb/^{235}U$	2σ	
34dr	416	1516	72.5	0.27	0.35947	0.01038	0.04945	0.00060	0.58	0.0126	0.0010	0.0527	0.0016	311.24	7.37	311.87	15.42	100
70c	19	273	11.7	0.07	0.42004	0.03381	0.04580	0.00095	0.55	0.0132	0.0015	0.0666	0.0055	288.79	11.71	356.13	47.55	81
70r	4	255	12.1	0.02	0.40385	0.02860	0.05204	0.00091	0.55	0.0146	0.0020	0.0563	0.0041	327.14	11.15	344.48	40.79	95
71c	60	382	16.8	0.16	0.33171	0.02083	0.04683	0.00075	0.55	0.0126	0.0014	0.0514	0.0033	295.13	9.23	290.92	31.44	101
71r	10	144	6.5	0.07	0.43035	0.03894	0.04821	0.00097	0.55	0.0124	0.0015	0.0648	0.0060	303.63	11.92	363.47	54.23	84
72c	10	78	3.4	0.12	0.42327	0.05477	0.04641	0.00122	0.54	0.0129	0.0015	0.0662	0.0087	292.55	15.02	358.43	76.08	82
72r	8	721	29.1	0.01	0.33103	0.01851	0.04442	0.00070	0.55	0.0126	0.0016	0.0541	0.0031	280.28	8.64	290.40	27.98	97
75c	147	650	29.0	0.23	0.33893	0.01800	0.04714	0.00071	0.55	0.0099	0.0012	0.0521	0.0029	297.04	8.74	296.41	27.06	100
75dr[e]	18	373	16.4	0.05	0.33748	0.01929	0.04811	0.00072	0.55	0.0124	0.0015	0.0509	0.0030	303.02	8.85	295.31	29.01	103
76c[e]	37	679	29.9	0.05	0.34947	0.01642	0.04813	0.00068	0.56	0.0124	0.0015	0.0527	0.0026	303.14	8.36	304.37	24.51	100
76r	10	322	13.6	0.03	0.33229	0.02301	0.04623	0.00078	0.55	0.0117	0.0015	0.0521	0.0037	291.44	9.61	291.36	34.67	100
77c[e]	11	166	7.3	0.07	0.35740	0.03290	0.04756	0.00092	0.54	0.0111	0.0015	0.0545	0.0051	299.63	11.32	310.32	48.43	97
77dr	11	571	24.8	0.02	0.35255	0.01788	0.04782	0.00070	0.55	0.0116	0.0015	0.0535	0.0028	301.23	8.61	306.68	26.61	98

[a] Concentration is approximately estimated based of the concentration of U and Th in GJ-1 standard (Jackson et al. 2004)

[b] Data not corrected for common-Pb

[c] Rho factor is calculated using the sum of relative 1σ % errors for $^{207}Pb/^{235}U$ and $^{206}Pb/^{238}U$ divided by the same plus sum of relative 1σ % error for $^{207}Pb/^{206}Pb$. The used formula is: = (1σ % error of $^{207}Pb/^{235}U$ + 1σ % error of $^{206}Pb/^{238}U$)/(1σ % error of $^{207}Pb/^{235}U$ + 1σ % error of $^{206}Pb/^{238}U$ + 1σ % error of $^{207}Pb/^{206}Pb$)

[d] Concordance calculated as (^{206}Pb–^{238}U age/^{207}Pb–^{235}Pb age) × 100

[e] Analyses used for concordia age calculation on Fig. 7

Table 2 U–Pb isotopic composition and dating of zircons from sample Kul 21

Zircon analysis	Th (ppm)	U (ppm)	Pb (ppm)	Th/U	Isotope ratio for Whederill plot[a,b]				Rho[c]	Isotope ratio[a,b]				Age estimate (Ma)				Concord-ance[d]
					$^{207}Pb/^{235}U$	1σ	$^{206}Pb/^{238}U$	1σ		$^{208}Pb/^{232}Th$	1σ	$^{207}Pb/^{206}P$	1σ	$^{206}Pb/^{238}U$	2σ	$^{207}Pb/^{235}U$	2σ	
Detrital																		
50	54	165	50	0.326	4.7652	0.13	0.2861	0.0037	0.59	0.0991	0.0091	0.1208	0.0034	1622.11	37.22	1778.80	43.1	91
117 core	18	177	47	0.099	3.7595	0.124	0.27408	0.0037	0.58	0.0794	0.0080	0.0996	0.0033	1561.59	37.37	1584.20	49.7	99
40	402	1164	188	0.345	1.5864	0.032	0.15737	0.0018	0.61	0.0516	0.0029	0.0731	0.0015	942.24	20.37	964.92	24.37	98
107	28	412	56	0.068	1.6571	0.078	0.14492	0.0023	0.57	0.0372	0.0057	0.0829	0.0040	872.53	25.65	992.31	57.02	88
110 core	91	330	28	0.276	0.7171	0.041	0.08665	0.0014	0.56	0.0257	0.0037	0.0600	0.0035	535.79	16.36	549.01	47.50	98
46	51	822	52	0.062	0.5206	0.016	0.06865	0.0009	0.58	0.0240	0.0019	0.0550	0.0017	428.13	10.49	425.62	20.63	101
63 core	128	324	16	0.395	0.4061	0.016	0.04937	0.0007	0.57	0.0167	0.0012	0.0597	0.0024	310.75	8.47	346.14	23.41	90
66 core	121	246	13	0.493	0.3646	0.021	0.04897	0.0008	0.56	0.0169	0.0012	0.0540	0.0032	308.28	9.83	315.71	31.42	98
66 rim[e]	253	451	23	0.560	0.3563	0.013	0.04863	0.0007	0.57	0.0154	0.0011	0.0531	0.0020	306.19	8.11	309.50	19.75	99
105 core	461	847	43	0.545	0.3951	0.02	0.04812	0.0007	0.56	0.0148	0.0016	0.0595	0.0030	303.06	8.73	338.10	28.14	90
63 dark rim[e]	201	619	29	0.325	0.3505	0.012	0.04770	0.0006	0.58	0.0148	0.0011	0.0533	0.0019	300.48	7.87	305.13	18.32	98
61 dark domain[e]	368	919	44	0.401	0.3477	0.01	0.04729	0.0006	0.59	0.0142	0.0009	0.0533	0.0015	297.96	7.26	303.00	14.72	98
111 rim[e]	430	2069	94	0.208	0.3563	0.014	0.04700	0.0006	0.57	0.0152	0.0022	0.0550	0.0022	296.18	7.63	309.46	21.08	96
63 oscillatory band[e]	201	653	31	0.309	0.3536	0.015	0.04694	0.0007	0.57	0.0159	0.0012	0.0546	0.0023	295.81	8.25	307.47	21.52	96
70a core	1468	2029	99	0.724	0.3159	0.011	0.04379	0.0006	0.58	0.0139	0.0011	0.0523	0.0019	276.36	7.29	278.79	16.97	99
51 core	408	1008	46	0.404	0.3203	0.011	0.04368	0.0006	0.58	0.0164	0.0016	0.0532	0.0018	275.70	7.04	282.21	16.17	98
61 oscillatory band	259	683	30	0.379	0.3103	0.009	0.04288	0.0005	0.58	0.0142	0.0009	0.0525	0.0016	270.75	6.67	274.48	14.55	99
121 rim	17	518	19	0.032	0.2780	0.017	0.04060	0.0006	0.55	0.0116	0.0013	0.0497	0.0031	256.66	7.56	249.14	26.72	103
121 core	17	133	5	0.126	0.2972	0.043	0.04016	0.001	0.54	0.0119	0.0013	0.0537	0.0079	253.93	11.89	264.24	66.40	96
110 rim	5	400	15	0.012	0.4053	0.034	0.04005	0.0009	0.55	0.0269	0.0144	0.0734	0.0063	253.25	11.03	345.54	48.37	73
Metamorphic																		
112 rim	7	258	6	0.025	0.1769	0.04	0.02648	0.001	0.54	0.0129	0.0115	0.0485	0.0111	168.59	12.3	165.43	67.54	102
56 sector rim	13	79	2	0.161	0.1785	0.031	0.02567	0.0007	0.53	0.0092	0.0017	0.0504	0.0088	163.50	8.54	166.82	52.37	98
56 white core	10	53	1	0.195	0.1687	0.037	0.02489	0.0008	0.53	0.0070	0.0019	0.0492	0.0108	158.59	9.81	158.33	62.86	100
43-2 core	589	282	10	2.091	0.2045	0.013	0.02415	0.0004	0.55	0.0080	0.0005	0.0614	0.0039	153.85	5.03	188.96	21.21	81
48 dark domain[6]	382	239	8	1.596	0.1726	0.014	0.02383	0.0004	0.55	0.0082	0.0007	0.0525	0.0044	151.86	5.54	161.68	24.32	94
47 grey domain[6]	32	205	5	0.154	0.1609	0.013	0.02375	0.0004	0.55	0.0100	0.0011	0.0491	0.0039	151.42	5.29	151.52	21.99	100
47 white rim[6]	41	196	5	0.207	0.1600	0.016	0.02367	0.0005	0.54	0.0116	0.0012	0.0490	0.0049	150.91	5.92	150.72	27.2	100
43-1 core[6]	1242	554	20	2.241	0.1720	0.009	0.02364	0.0004	0.56	0.0077	0.0004	0.0528	0.0027	150.63	4.41	161.23	14.72	93
48 white domain[6]	184	129	4	1.424	0.1597	0.017	0.02359	0.0005	0.54	0.0078	0.0007	0.0491	0.0053	150.35	5.92	150.52	29.71	100
47 dark domain[6]	946	596	19	1.589	0.1532	0.007	0.02306	0.0003	0.57	0.0078	0.0006	0.0482	0.0021	147.01	4.03	144.75	11.58	102
104	74	231	5	0.321	0.2106	0.038	0.02258	0.0007	0.54	0.0075	0.0012	0.0676	0.0124	144.04	8.95	194.14	62.7	74
57 dark core	1	217	4	0.005	0.1517	0.014	0.02256	0.0004	0.54	0.0051	0.0147	0.0488	0.0046	143.93	5.55	143.45	24.95	100
67 dark core	45	590	6	0.077	0.0750	0.005	0.01159	0.0002	0.55	0.0040	0.0006	0.0469	0.0032	74.39	2.29	73.46	9.61	101

Table 2 continued

Zircon analysis	Th (ppm)	U (ppm)	Pb (ppm)	Th/U	Isotope ratio for Whederill plot[a,b]				Rho[c]	Isotope ratio[a,b]				Age estimate (Ma)				Concord-ance[d]
					$^{207}Pb/^{235}U$	1σ	$^{206}Pb/^{238}U$	1σ		$^{208}Pb/^{232}Th$	1σ	$^{207}Pb/^{206}P$	1σ	$^{206}Pb/^{238}U$	2σ	$^{207}Pb/^{235}U$	2σ	
51 dark left	15	4951	48	0.003	0.0704	0.002	0.01078	0.0001	0.59	0.0037	0.0013	0.0474	0.0014	69.23	1.7	69.09	3.81	100
51 dark right	7	2099	20	0.003	0.0692	0.003	0.01065	0.0002	0.57	0.0214	0.0039	0.0471	0.0021	68.40	1.9	67.95	5.71	101
67 white rim	20	375	4	0.055	0.1024	0.008	0.01065	0.0002	0.55	0.0105	0.0013	0.0698	0.0057	68.40	2.9	99.05	14.92	69
58 dark rim	0	17	0	0.022	0.0738	0.13	0.01031	0.0013	0.52	0.0591	0.0525	0.0519	0.0918	66.23	16.2	72.31	231.5	92
Mixed ages																		
45	81	100	2	0.815	0.1442	0.025	0.02065	0.0006	0.53	0.0077	0.0006	0.0507	0.0090	131.84	7.07	136.85	44.5	96
57 white rim	23	83	2	0.274	0.3099	0.038	0.01922	0.0007	0.55	0.0189	0.0018	0.1169	0.0147	122.82	8.6	274.17	57.41	45
70a rim	110	638	17	0.173	0.1991	0.01	0.02738	0.0004	0.56	0.0104	0.0010	0.0527	0.0027	174.23	5.27	184.42	16.87	94
105 rim	458	1304	59	0.351	0.3578	0.014	0.04525	0.0006	0.57	0.0138	0.0015	0.0574	0.0023	285.39	7.28	310.65	21.16	92
109 core	58	596	11	0.096	0.1559	0.015	0.01947	0.0004	0.54	0.0069	0.0013	0.0581	0.0058	124.41	5.18	147.16	26.55	84
109 rim	58	122	2	0.471	0.1103	0.057	0.01600	0.0009	0.52	0.0093	0.0017	0.0500	0.0260	102.42	11.67	106.28	101.5	96
112 core	494	855	31	0.578	0.2596	0.015	0.03389	0.0005	0.56	0.0104	0.0017	0.0556	0.0032	214.93	6.61	234.38	23.53	92
113 core	111	309	11	0.360	0.2761	0.024	0.03640	0.0007	0.55	0.0117	0.0019	0.0550	0.0049	230.58	8.46	247.57	37.99	93
113 rim	80	358	13	0.222	0.2668	0.027	0.03677	0.0008	0.54	0.0138	0.0024	0.0526	0.0053	232.88	9.45	240.15	42.26	97
114 core	119	572	16	0.207	0.1908	0.016	0.02862	0.0005	0.55	0.0099	0.0019	0.0484	0.0040	182.01	6.39	177.36	26.53	103
114 dark rim	17	1866	37	0.009	0.1894	0.01	0.02091	0.0003	0.56	0.0784	0.0154	0.0657	0.0035	133.52	4.17	176.15	17.14	76
114 white band	24	201	7	0.120	0.3011	0.03	0.03755	0.0008	0.54	0.0078	0.0010	0.0582	0.0059	237.73	9.32	267.29	46.45	89

[a] Concentration is approximately estimated based of the concentration of U and Th in GJ-1 standard (Jackson et al. 2004)

[b] Data not corrected for common-Pb

[c] Rho factor is calculated using the sum of relative 1σ % errors for $^{207}Pb/^{235}U$ and $^{206}Pb/^{238}U$ divided by the same plus sum of relative 1σ % error for $^{207}Pb/^{206}Pb$. The used formula is: = (1σ % error of $^{207}Pb/^{235}U$ + 1σ % error of $^{206}Pb/^{238}U$)/(1σ % error of $^{207}Pb/^{235}U$ + 1σ % error of $^{206}Pb/^{238}U$ + 1σ % error of $^{207}Pb/^{206}Pb$)

[d] Concordance calculated as ($^{206}Pb–^{238}U$ age/$^{207}Pb–^{235}Pb$ age) × 100

[e] Analyses used for concordia age calculation on Fig. 9c

[6] Analyses used for concordia age calculation on Fig. 9d

Table 3 U–Pb isotopic composition and dating of zircons from sample Kul 6

Zircon analysis	U (ppm)[a]	Pb (ppm)[a]	Th/U[a]	Isotope ratios							Ages (Ma)						Concordance
				$^{207}Pb/^{235}U$[b]	2 σ (%)[d]	$^{206}Pb/^{238}U$[b]	2 σ (%)[d]	rho[c]	$^{207}Pb/^{206}Pb$[e]	2 σ (%)[d]	$^{207}Pb/^{235}U$	2 σ	$^{206}Pb/^{238}U$	2 σ	$^{207}Pb/^{206}Pb$	2 σ	
7	73	21	0.75	3.3180	3.0	0.2495	2.6	0.89	0.0964	1.4	1485	44	1436	38	1556	13	97
8	204	60	0.50	3.6060	2.7	0.2642	2.5	0.93	0.0990	1.0	1551	42	1511	38	1605	9	97
9	43	11	0.68	2.4964	3.4	0.2173	2.6	0.74	0.0833	2.3	1271	44	1267	33	1277	22	100
10	453	132	0.43	3.6642	2.6	0.2699	2.5	0.96	0.0985	0.7	1564	41	1540	39	1595	7	99
11	401	79	0.47	1.9983	2.8	0.1845	2.6	0.93	0.0785	1.0	1115	31	1092	29	1160	10	98
12	342	35	0.57	0.7732	2.9	0.0938	2.5	0.87	0.0598	1.5	582	17	578	15	596	16	99
13	229	71	0.28	4.3774	2.6	0.2990	2.4	0.95	0.1062	0.8	1708	44	1686	41	1735	7	99
14	656	107	0.04	1.7820	2.9	0.1722	2.6	0.89	0.0751	1.3	1039	30	1024	26	1070	13	99
15	60	7	0.82	0.7706	3.9	0.0937	2.7	0.69	0.0596	2.8	580	23	577	16	590	31	100
16	137	15	0.88	0.7779	3.3	0.0945	2.4	0.72	0.0597	2.3	584	19	582	14	593	25	100
20	257	76	0.22	4.2188	2.7	0.2914	2.5	0.93	0.1050	1.0	1678	45	1649	41	1714	9	98
21	247	53	0.27	3.4879	3.3	0.1997	2.8	0.85	0.1267	1.7	1524	50	1174	33	2052	15	77
22	156	16	0.59	0.7747	3.5	0.0944	2.7	0.79	0.0595	2.1	582	20	581	16	587	23	100
24	217	43	0.38	2.0355	2.9	0.1904	2.7	0.92	0.0775	1.2	1127	33	1124	30	1135	12	100
25	247	25	0.11	1.0424	3.1	0.1028	2.7	0.84	0.0736	1.7	725	23	631	17	1030	17	87
26	671	243	1.14	3.8649	2.8	0.2857	2.7	0.96	0.0981	0.8	1606	45	1620	43	1589	7	101
28	106	16	1.41	0.9805	3.3	0.1130	2.5	0.76	0.0629	2.2	694	23	690	17	706	23	99
29	124	29	0.31	2.6564	3.2	0.2261	2.8	0.90	0.0852	1.4	1316	42	1314	37	1321	14	100
33	701	74	0.72	0.7713	2.6	0.0941	2.4	0.92	0.0595	1.0	581	15	580	14	584	11	100
34	759	69	0.16	0.7733	2.9	0.0944	2.5	0.88	0.0594	1.4	582	17	581	15	582	15	100
36	581	300	0.63	9.8145	2.5	0.4415	2.4	0.97	0.1612	0.6	2418	60	2358	57	2468	5	98
37	687	356	0.43	10.2382	3.4	0.4655	3.3	0.96	0.1595	1.0	2457	83	2464	80	2451	8	100
38	150	53	0.43	5.0019	2.9	0.3253	2.7	0.93	0.1115	1.1	1820	53	1816	49	1824	10	100
39	59	14	1.27	1.9849	4.3	0.1845	3.6	0.83	0.0780	2.4	1110	48	1091	39	1148	24	98
40	78	11	0.91	1.0427	3.5	0.1179	2.6	0.73	0.0641	2.4	725	26	718	19	747	26	99
41	246	74	0.41	3.8204	3.3	0.2790	3.1	0.94	0.0993	1.1	1597	52	1586	49	1611	11	99
42	144	50	0.33	5.0470	2.9	0.3294	2.7	0.93	0.1111	1.1	1827	54	1836	50	1818	10	100

[a] U and Pb concentrations and Th/U ratios are calculated relative to GJ-1 reference zircon

[b] Corrected for background and within-run Pb/U fractionation and normalised to reference zircon GJ-1 (ID-TIMS values/measured value); $^{207}Pb/^{235}U$ calculated using $(^{207}Pb/^{206}Pb)/(^{238}U/^{206}Pb \times 1/137.88)$

[c] Rho is the error correlation defined as the quotient of the propagated errors of the $^{206}Pb/^{238}U$ and the $^{207}/^{235}U$ ratio

[d] Quadratic addition of within-run errors (2 SD) and daily reproducibility of GJ-1 (2 SD)

[e] Corrected for mass-bias by normalising to GJ-1 reference zircon (~0.6 per atomic mass unit) and common Pb using the model Pb composition of Stacey and Kramers (1975)

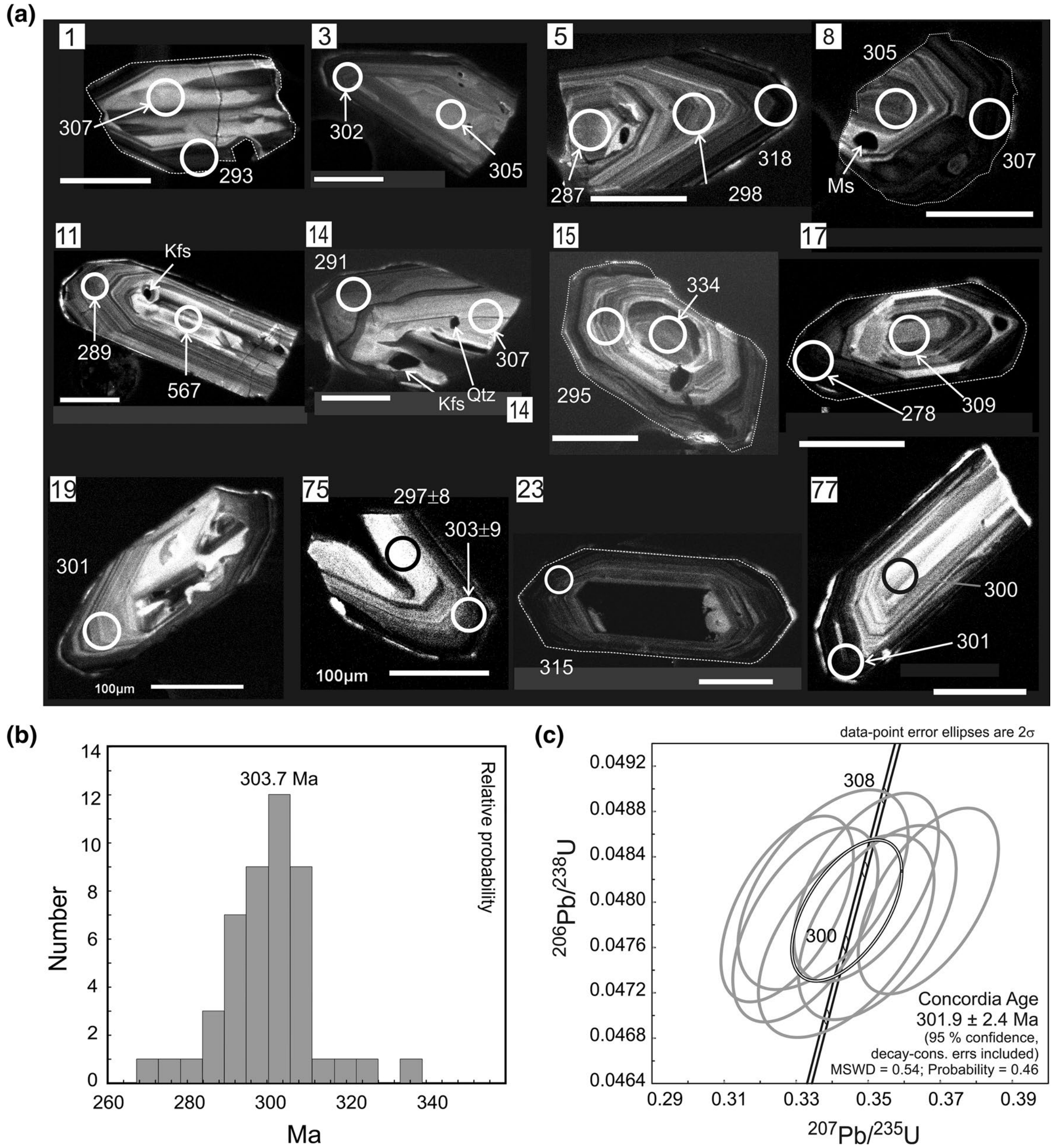

Fig. 7 Selected CL images (**a**) and dating results (**b**, **c**) of zircons from sample Kul-22, the augengneiss from Unit I. **a** *Circles* and nearby *numbers* denote analysis spots and ages ($^{206}Pb/^{238}U$ Ma). The *numbers* in white rectangles correspond to zircon analysis in Table 1: grains with xenocrystic cores (images 11, 15); mineral inclusions (images 11, 14, 8); homogenised oscillatory domains (images 1, 3, 14); anomalously old age of zircon rims (images 23, 5, 8, 77). The *scale bar* is 100 µm. **b** Probability density plot of $^{206}Pb/^{238}U$ ages. **c** Concordia diagram of Late Paleozoic protolithic zircon

Data on trace elements in selected spots from dated zircons [Appendix C (ESM)] help understanding the origin of the zircons. Chondrite-normalised REE patterns (Fig. 8) show uniform distribution with negative Eu- and positive Ce-anomalies, and steep HREE enrichment (LuN/GdN from 22 to 66). These are characteristic of continental crustal zircon populations of igneous or anatectic origin (Hoskin and Schaltegger 2003). We suggest a magmatic protolith origin since there are no signs of migmatisation in the rock. The variation of Th/U ratios between 1.67 and 0.01 with core-to rim decrease in the majority of dated grains (Table 1) indicates partial redistribution of Th and U due to metamorphism and/or interaction with metamorphic fluids.

The whole-rock major element geochemistry corresponds to peraluminous granite with high silica content of 70.97 %, a sum of alkali oxides of 7.45 % (TAS diagram not shown), and A/CNK of 1.14 [Appendix D (ESM)]. Two

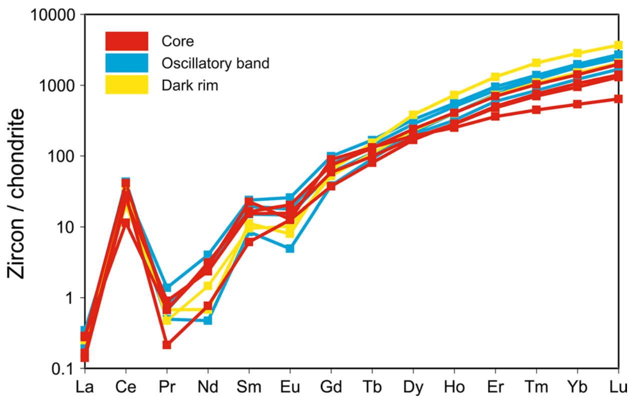

Fig. 8 Chondrite-normalised REE patterns of zircon from sample Kul-22

muscovite inclusions [Si 3.10 and 3.34 pfu; Appendix E (ESM)] in oscillatory zoned domains of dated zircons indicate pressure conditions of zircon growth or metamorphic overprint of 0.5–1.1 GPa above granite solidus temperature of 650 °C (based on Simpson et al. 2000). The contents of Ti [Appendix C (ESM)] are below detection limits, which precludes an application of Ti-in-zircon thermometry and better estimate of thermal conditions.

KUL-21 (garnet-chlorite-mica-schist from Unit II)

The scanty zircon population from Kul-21 comprises small fragments and rounded short-prismatic whole grains (<0.15 mm commonly, elongation ≤2), colourless to pale yellowish and transparent. The CL and BSE images show complex internal structures (Fig. 9a): xenocrystic cores (image 110); sector and oscillatory zoning cut off by areas of re-homogenised zircon (image 105), bands of homogeneously textured zircon (image 110); patchy zoning (images 63, 66, 47, 70a) with bright seams indicating altered fractures disrupting original zoning (images 63, 66, 110). Most of the internal structures reflect variations in the physico-chemical conditions and are caused by modifications of pre-existing structures and/or by growth of new zircon.

The zircon ages vary between ca. 1600 Ma and ca. 70 Ma (Table 2), clustering at 69 Ma, 150 Ma, and from 220 to 310 Ma (Fig. 9b). Older ages appear in single detrital zircon grains (Fig. 9a; images 50, 107) or xenocrystic cores (image 11). The detrital zircons suggest different source lithologies among which dominated Late Paleozoic igneous or anatectic ones. The ages scattering between 310 and 250 Ma belong to zircons that keep partially magmatic oscillatory or sector zoning, strongly affected by recrystallization or new metamorphic growth (Fig. 9a). Some of them contain inclusions of quartz, plagioclase, biotite and muscovite. Six spots, whose U–Pb data overlap within 2σ error, yield a weighted mean age of 299.7 ± 3.2 Ma and a concordia age 299.9 ± 1.8 Ma (Fig. 9c; Table 2). Other three grains yield a concordia age of 273.6 ± 2.0 Ma (1σ, MSWD 1.2; not shown). The variation of Th/U ratio values between 0.2 and 0.7 in these zircons (Table 2) are consistent with magmatic origin. One chondrite-normalised REE pattern of 300 Ma old grain [Fig. 10, zircon grain 66 in Appendix C (ESM)] shows features of magmatic or anatectic zircon with positive Ce- and negative Eu-anomaly 0.42, and HREE enrichment with LuN/GdN 32.

The Late Jurassic zircons are present as single grains or domains in composite grains of metamorphic internal structure (Fig. 9a, images 43, 47, 48, 57). Quartz and apatite inclusions are common. The ages scatter between 120 and 160 Ma (Table 2). Five spots in three grains yield a concordia age of 149.7 ± 0.97 Ma (Fig. 9d).The contents of trace elements [data in Appendix C (ESM)] resemble magmatic or high-grade metamorphic zircons that have grown in the presence of melt (Rubatto 2002). Chondrite-normalised REE patterns (Fig. 10) show positive Ce-and negative Eu-anomaly (0.14–0.37), variable LuN/GdN (8–63) and Th/U ratios (0.15–2.2; Table 2). The contents of Ti are below the detection limit, except for one zircon grain [analysis 69, with 22.7 ppm Ti; Appendix C (ESM)]. The result of Ti-in zircon thermometry for this grain is 854 °C (after Ferry and Watson 2007).

Three grains only represent the youngest zircon generation of metamorphic internal structures and origin (Fig. 9a, images 51, 58, 67). Five spots in these grains have weighted mean age of 69.9 ± 3.2 and four of them yield two concordant ages at 74 and 68–69 Ma (Fig. 9e; Table 2). The composition [Appendix C (ESM)] is distinguished by low contents of trace elements, except for Hf, variable U contents and low Th/U ratios (<0.1; Table 2). The distribution of REE (Fig. 10) exhibits different patterns. The older zircon (grain 67) differs with negative Eu-anomaly and low LuN/GdN = 2.4, suggesting crystallization in competition with feldspar and HREE-rich garnet, e.g. upper amphibolite or granulite facies. Two spots in the younger zircon grain 51 show no or very weak Eu anomalies and high LuN/GdN values (163 and 223), suggesting growth at high pressure outside the feldspar stability field. The zircon grain 58 has similar features (LuN/GdN = 140), though all REE contents are lower. The content of Ti is 16.5 ppm in zircon grain 51, corresponding to 819 °C (after Ferry and Watson 2007).

The whole-rock geochemistry [Appendix D (ESM)] suggests a sedimentary protolith of greywacke to litharenite composition. The PerpleX-generated pseudosection (Connolly 2005) predicts a large stability field for the higher-grade chlorite-free assemblages

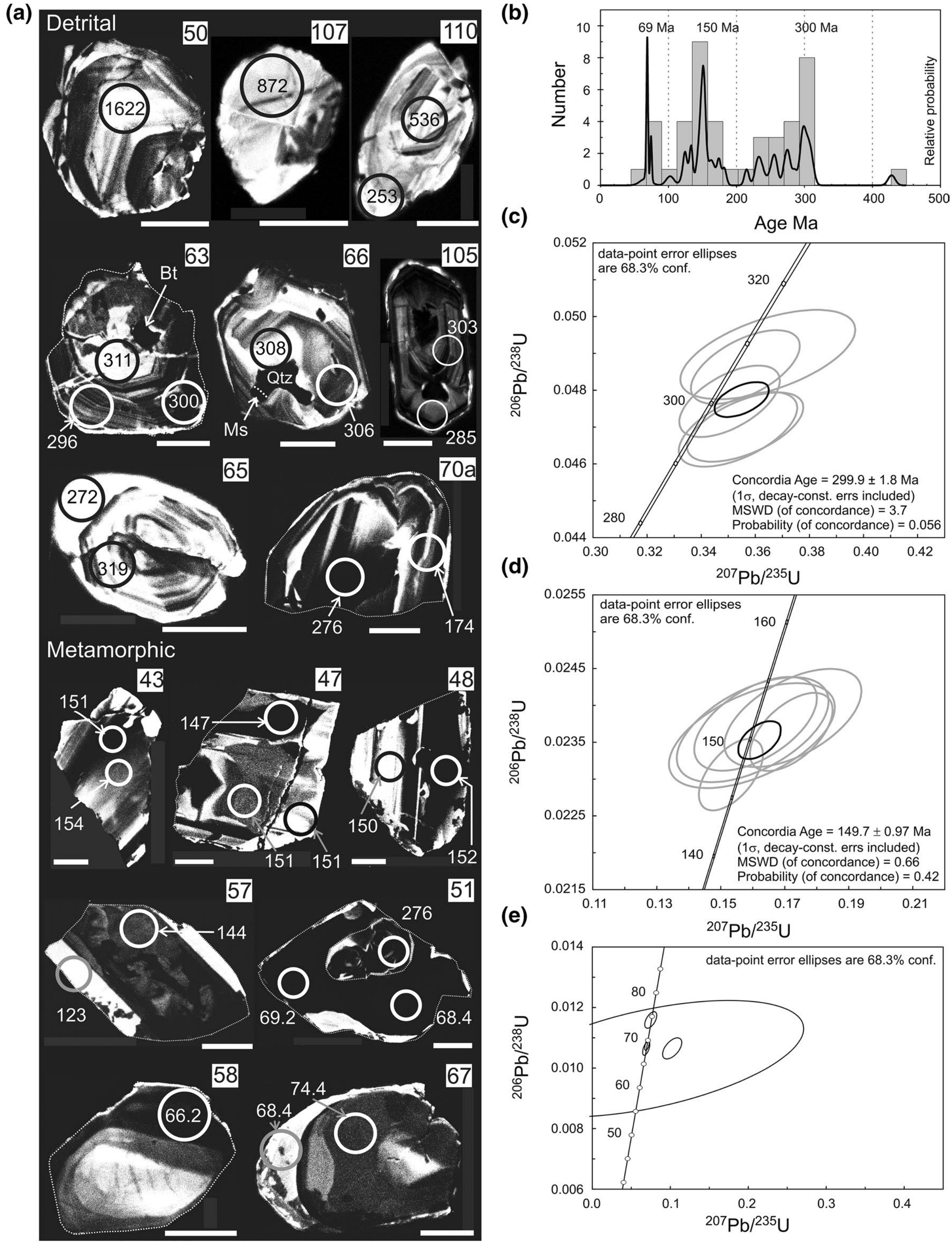

Fig. 9 Selected CL images (**a**) and dating results (**b–e**) of zircons from sample Kul-21, the garnet-bearing schist from Unit II. **a** The CL images show old detrital single grains (46, 50, 107) and xenocrystic core (110); Late Paleozoic detrital grains (63, 66, 105) with younger metamorphic overgrowth (70a); metamorphic Late Jurassic zircon (47, 48, 43) with younger metamorphic rim (57); metamorphic Late Cretaceous zircon (51, 58, 67).The *scale bar* is 50 μm. **b** Probability density plot of $^{206}Pb/^{238}U$ ages. (-cb) Concordia diagram of detrital late Paleozoic group zircons. **d** Concordia diagram of metamorphic Late Jurassic zircon. **e** Concordia diagram of metamorphic Late Cretaceous zircon

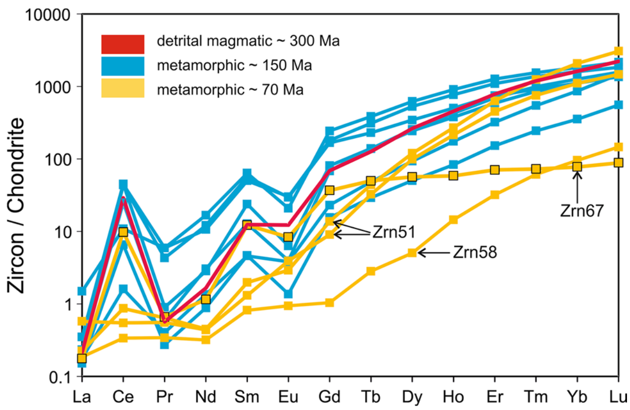

Fig. 10 Chondrite-normalised REE patterns of zircon from sample Kul-21

(570–850 °C/0.4–2.0 GPa; Fig. 11) corresponding with amphibolite to high-pressure granulite facies. Chlorite appears below 550 °C. The calculated retrograde assemblage contains ilmenite and zoisite, the participation of which in the sample is not supported by strong evidence, except for the observation of opaque minerals and epidote. Tourmaline was not considered because of the lack of thermodynamic data. The comparison between calculated phengite component (Fig. 11), the composition of muscovite inclusions [Si 3.26 pfu; Appendix E (ESM)] and the result of Ti-in-zircon thermometry suggests 850 °C/1.6 GPa as conditions of Late Jurassic zircon growth, most probably in the presence of melt and related with the first mineral assemblage of garnet porphyroblasts. Although contradictory, data available on the youngest zircon generations (74 and 68–69 Ma) support an interpretation of changing metamorphic conditions and a transition from a feldspar- and garnet-bearing assemblage for zircon core spot 67c (74 Ma) towards a feldspar-free assemblage for zircon spots in grain 51 (68–69 Ma). Having in mind the result of Ti-in zircon thermometry (819 °C), such a PT path suggests cooling at ca. 2 GPa (Fig. 11).

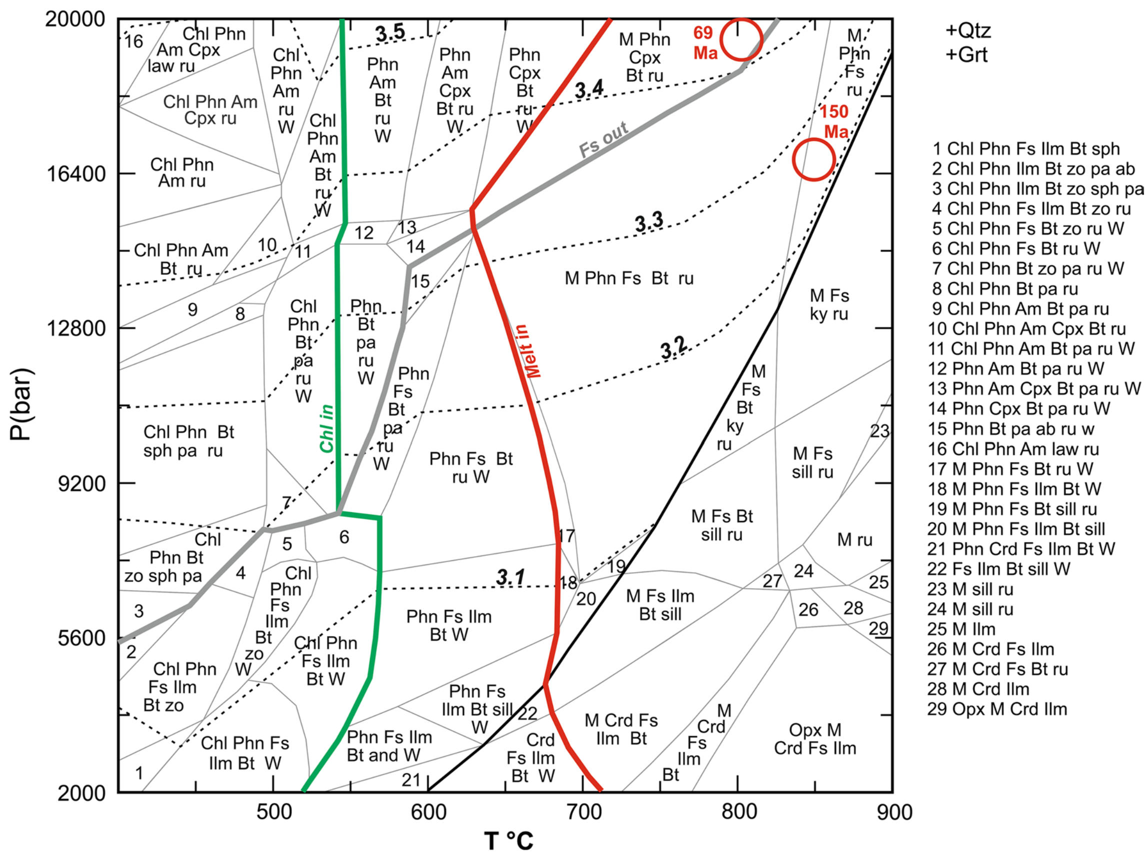

Fig. 11 P–T pseudosection calculated with PERPLE_X for sample Kul 21 (Table 3). *Dashed lines* denote Si-isopleths in phengite. The *red circles* correspond to the estimates of possible zircon growth conditions: a combination of Ti-in-zircon thermometry 850 °C and Si-in-phengite isopleths (Si 3.26 pfu for muscovite inclusion in 150 Ma old zircon); and Ti-in-zircon thermometry 819 °C for 68–69 Ma old zircon, whose REE pattern suggests feldspar-free environment of growth. All assemblages contain quartz (Qtz) and garnet (Grt). Other mineral abbreviations: *ab* albite, *Am* amphibole, *and* andalusite, *Bt* biotite, *Chl* chlorite, *Cpx* clinopyroxene, *Crd* cordierite, *Ilm* ilmenite, *ky* kyanite, *law* lawsonite, *M* melt, *Opx* orthopyroxene, *pa* paragonite, *Phn* phengite, *ru* rutile, *sill* sillimanite, *sph* titanite, *W* water, *z* zoisite

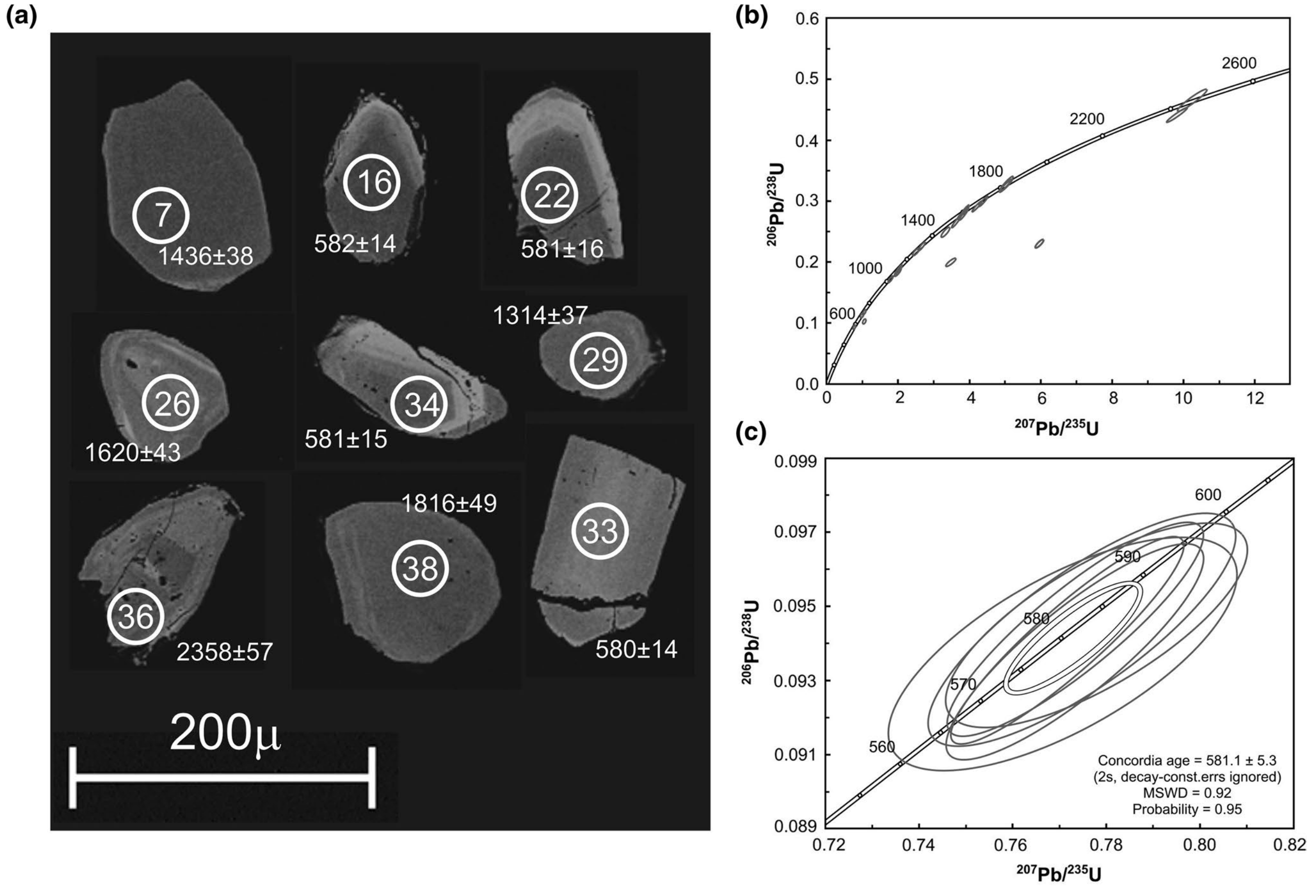

Fig. 12 Backscattered-electron images of zircons (**a**) and dating results from Kul-6, the muscovite gneiss from Unit IV: **b** concordia diagram of all dated grains; **c** concordia diagram of the youngest zircon grains

KUL 6 (Muscovite gneiss from Unit IV)

Zircons from the muscovite gneiss are brownish-pink to pale pink to colourless and almost inclusion-free. They are short- to medium-prismatic and partly rounded. Many crystals appear almost homogeneous in backscatter electron (BSE) images, others show weak, euhedral BSE zoning, partly truncated by the rounded outline (Fig. 12). Some zircons have BSE-light rims along their rounded outline, suggesting a metamorphic rim. U contents vary between 43 and 759 ppm, Th/U ratios are strongly variable between 0.04 and 1.41 (Table 3) indicative of differences in the origin of zircon grains. The six zircons of the youngest age population (see below) are of magmatic type based on their BSE zoning (Fig. 12) and have U contents between 60 and 759 ppm, and Th/U ratios between 0.16 and 0.88. The zircon ages vary between ca. 580 Ma and ca. 2400 Ma but fall into distinct age groups (Table 3). The youngest of these, including six grains, is homogeneous and yields a very well-defined concordia age of 581.1 ± 5.3 Ma. It is interpreted as the crystallization age of the magmatic protolith. The other grains are interpreted as inherited. Four of them have ages around 700 Ma, five grains fall between 1 and 1.4 Ga, nine grains are between 1.5 and 1.9 Ga old. Two grains have ages between 2.4 and 2.5 Ga. The metamorphic overprint that transformed the granite into a gneiss is probably recorded by the BSE-light rims (Fig. 12). These are, however, too narrow for dating.

Discussion

Correlation of tectonic units

The dating results allow a rather clear correlation of Unit I and II to certain levels of the Rhodope nappe stack. The Late Carboniferous protolith age of the augengneiss from Unit I, 301.9 ± 2.4 Ma, supports its correlation with the lower high-grade basement (Lower Allochthon) cropping out south of the study area in the Byala Reka-Kechros Dome. On orthogneiss from that area, an identical protolith age of 301 ± 4 Ma was determined using U–Pb SHRIMP on zircon (Carrigan et al. 2003). Similar ages between 296 and 320 Ma with larger errors were obtained from orthogneisses of the Byala Reka-Kechros Dome by Peytcheva et al. (1992, 1998) and Peytcheva and von Quadt (1995). The top-south mylonite shear sense observed in Unit I is also the same as observed in gneisses of the Byala Reka-Kechros Dome (Bonev et al. 2010c).

The analysed garnet-bearing schist from Unit II is a high-grade metamorphic rock of amphibolite to granulite facies, as indicated by pseudosection modelling (Fig. 11) and Ti-in-zircon thermometry. The whole-rock composition identifies it as a metasediment. Zircons with typical magmatic features clustering at 310, 275, 250 and 150 Ma old metamorphic zircons suggest that the clastic sedimentary protolith formed between Permian and Jurassic from the erosion of a source area rich in Late Variscan granitoids. This rock was metamorphosed at ca. 150 Ma (Late Jurassic) under conditions of ca. 850 °C/1.4 GPa, probably in the presence of anatectic melt. A second event of high-grade metamorphism took place in the Late Cretaceous between 74 and 68 Ma.

A migmatitic orthogneiss from the Krumovitsa-Kimi Unit of the Upper Allochthon, 40 km southwest of our study area, yielded an amazingly similar age spectrum as our sample Kul-21 (Liati et al. 2015). These authors calculated concordia ages for the zircon domains in their sample at 268 ± 7 Ma, 157.7 ± 2.3 Ma, and 73.8 ± 0.8 Ma. The Permian age is interpreted to date protolith crystallization, the other two as representing HP to UHP metamorphism. Similar ages were determined in earlier studies of the Krumovitsa-Kimi Unit (see review by Liati et al. 2011). The difference between Kul-21 and the Liati et al. (2015) sample is that the protoliths are sedimentary and magmatic rocks, respectively, but the timing of the metamorphic overprint is identical. We assume that the Jurassic and Late Cretaceous zircon ages belong to two separate subduction-exhumation cycles (see Liati et al. 2011 and Froitzheim et al. 2014).

Because of the similar metamorphic history, the analogous tectonic position on top of the Lower Allochthon, and the similar lithological association (gneiss, amphibolite, marble, ultramafic rock) we can firmly correlate Unit II with the Krumovitsa-Kimi Unit of the Upper Allochthon. A correlation with the low-grade Mesozoic unit or Uppermost Allochthon, as suggested by Bonev et al. (2010a), is not supported by our results. The Uppermost Allochthon is in the Kulidzhik area only represented by Unit III.

The age spectrum from the muscovite gneiss of Unit IV is strongly different from the one of Unit I and the Lower Allochthon in the Eastern Rhodopes in general. It is therefore improbable that the gneisses of the Kulidzhik klippen (our Unit IV) were originally a piece of the lower high-grade unit (our Lower Allochthon/Unit IV) as interpreted by Bonev et al. (2010c). Gneisses with a similar age spectrum are unknown from the Eastern Rhodopes and correlatives have to be sought for outside this area. In the Circum-Rhodope Belt in Chalkidiki (Greece), an orthogneiss sliver cropping out at Pirgidakia yielded zircon protolith ages of 570.0 ± 7.0 Ma and 587.6 ± 3.4 Ma (Himmerkus et al. 2006), very similar to the crystallization age of the protolith of our sample, 581 ± 5 Ma. Like Unit IV, the orthogneiss sliver of Pirgadikia rests on strongly deformed low-grade metamorphic rocks of the Uppermost Allochthon and these in turn rest on the basement of the Upper Allochthon, in this case, the Vertiskos Unit of the Serbo-Macedonian Massiv (Fig. 2 of Himmerkus et al. 2006). Since the Uppermost Allochthon is assumed to be derived from Jurassic-age arc- and backarc oceanic crust of Neotethys which was emplaced northward on the European margin (Upper Allochthon) during an arc-continent collision (e.g. Bonev et al. 2015; Froitzheim et al. 2014), the origin of Unit IV and the Pirgadikia gneisses might be a continental fragment in the Neotethys. However, this is highly speculative. At some point, Unit IV must have been thrust over the much younger rocks of Unit III, but we are unable to reconstruct the kinematics of this thrusting due to the pervasive brittle overprint related to extensional detachment faulting (see below). Correlating Unit IV with other gneiss units of the Rhodope Nappe stack (be it the Lower, Middle, or Upper Allochthon) is also precluded by the two Jurassic $^{40}Ar–^{39}Ar$ cooling ages, ca. 154 Ma and ca. 157 Ma, determined on Unit IV orthogneiss by Bonev et al. (2010a). Such old cooling ages have never been reported for the Lower, Middle, and Upper Allochthon.

Tectonic evolution

Unit I was pervasively mylonitised with a top-south to -southwest shear sense. Orthogneisses with the same penetrative mylonitic structure and top-southwest sense of shear compose the core of Byala Reka-Kechros Dome (Lower Allochthon) further south. There the southward kinematics was previously correlated with two different events: Late Cretaceous top-south thrusting (Burg et al. 1996; Ivanov 1998; Bonev 2006b; Sarov et al. 2008) and Late Eocene top-south extensional detachment faulting (Krohe and Mposkos 2002; Bonev et al. 2006b). For our study area, three options exist: either the top-south fabric entirely results from Cretaceous or Paleogene thrusting, or it is entirely related to Eocene extension, or it is related partly to one, partly to the other process. We favour the second option, an entirely extensional nature of the observed shear fabric, for the following reasons: (1) there is no evidence for a break in the evolution of top-south shearing; (2) the mylonites developed under decreasing temperatures, beginning under conditions that allowed dynamic recrystallization of feldspar and grain-boundary migration in quartz, i.e. conditions around 500 °C, and continuing under decreasing temperatures down to less than ca. 400 °C when biotite was replaced by chlorite. This fits an extensional better than a compressional process. Therefore, we link the top-south shearing in Unit I with the top-southwest, mylonitic to brittle, extensional, Paleogene-age Kechros Detachment Fault (Krohe and Mposkos 2002; Bonev et al. 2006b) along which the Byala Reka-Kechros Dome was exhumed further south.

Unit II is dominated by greenschist facies, top-north mylonitic to cataclastic shearing. The upward-increasing intensity of mylonitisation, chloritisation, and cataclastic overprint of the mylonites, eventually leading to the "cap" of cataclasite at the top of Unit II, all suggest that these phenomena belong to extensional shearing under decreasing temperatures, progressively localised at the top of Unit II which therefore represents a top-north extensional detachment fault. The same top-north shearing also moderately affected Unit I where it is represented by ductile to brittle shear zones overprinting the top-south mylonites (Fig. 2).

Only a few tens of metres above the detachment surface capping Unit II, and locally less, follows the brittle basal contact of Unit IV, characterised by cohesionless kakirites. Both detachments, between units II and III and the one at the base of Unit IV, were active under brittle conditions, but the latter one at still lower temperatures, as can be seen from the chlorite-poor and cohesionless fault rocks at the upper detachment, in contrast to the pervasive chloritisation and cohesive cataclasite at the lower detachment. In Unit III, low-temperature calcite mylonites with a top-north shear sense are kinematically identical to the mylonites and cataclasites in Unit II. Therefore, we assume that Unit III is also part of the extensional fault system and that the "real" top detachment is the one located at the base of Unit IV. This fault juxtaposes either units III and IV or directly units II and IV. We propose to call the main extensional fault at the bottom of Unit IV the Kulidzhik Detachment (Fig. 2—the map and cross section). The Kulidzhik Detachment and the fault zone at the top of Unit II are conjugated structures that are in a kinematic continuum. These two faults must be assumed as of the same age and most probably concomitant with the top-to-the north greenschist facies shear zone at the boundary between units I and II, whereas units I to III were exhumed by the two detachments to variable amounts, Unit IV, in the hanging wall of the Kulidzhik detachment, was already at a shallow crustal level since it cooled in the Late Jurassic.

An upper age limit for the detachment system is represented by the sealing sediments of the Podrumche Formation, presumably Late Eocene in age. The exact age of these sediments is not biostratigraphically constrained in the study area but the Madzharovo volcanic rocks, resting on top of the Podrumche Formation, are well dated (ca. 32.7–32.2 Ma; Marchev and Singer 2002) and clearly postdate detachment faulting. On the other hand, 42–36 Ma $^{40}Ar/^{39}Ar$ muscovite cooling ages from gneisses in the Byala Reka-Kechros Dome (Lips et al. 2000) show that extensional unroofing, with top-southwest kinematics in the Byala Reka-Kechros area, was going on at that time and probably started a few Ma earlier. We assume that the extensional deformation in our study area, including top-south shearing in Unit I and top-north shearing in units I, II, and III, as well as the detachment surfaces at the top of Unit II and at the base of Unit IV, was active between ca. 45 and ca. 33 Ma. The greenschist facies mylonitization of Unit II postdated the Late Cretaceous (~74–68 Ma) high-grade metamorphic mineral assemblage. Due to the similar kinematics and shearing conditions, the retrogression of Unit II must be linked to the extensional event that exhumed the core of Byala Reka dome as was already proposed by Sarov et al. (2008).

North-dipping extensional detachments, similar in age and kinematics to the Kulidzhik detachment, occur all along the northern border of the Rhodopes. These include the Tokachka Detachment at the northern border of the Kesebir-Kardamos Dome (Bonev et al. 2006a), the Kyuse Hasanlartepesi Detachment in the eastern Central Rhodopes (Pleuger et al. 2011), the Rila-Pastra Normal Fault (Tueckmantel et al. 2008) and the Djerman Detachment (Shipkova and Ivanov 2000) in the Rila area. South- and southwest-dipping detachments occur as well: the Kerdilion and Mesta detachments (Kilias et al. 1999; Burchfiel et al. 2003; Brun and Sokoutis 2007; Georgiev et al. 2010), the Kechros detachment (Krohe and Mposkos 2002), and others. These are more typical for the southern and southwestern parts of the Rhodopes. However, since we correlated top-south shearing in Unit I with Eocene extension, it follows that top-south extensional shearing also occurs at the northern border of the Rhodopes. The Kerdilion, Mesta, and Kechros detachments are Late Eocene to Oligocene in age, just like the Kulidzhik and other north-dipping detachments. In addition, a major southwest-dipping detachment southwest of the Rhodopes was active in the Miocene, the Strymon Valley Detachment Fault (Dinter 1998). Together, these detachment systems accommodated the two-sided exhumation of deep parts of the thickened orogenic crust, resulting in the core complexes where the Lower Allochthon became exposed.

The overprinting relations between top-south and top-north fabrics observed in the Kulidzhik area suggest that unroofing of deep orogenic crust in the Eastern Rhodopes evolved from asymmetric to symmetric, as schematically shown in Fig. 13. In an early stage, extension was asymmetric and governed by a south-dipping detachment fault and related ductile shear zone. The

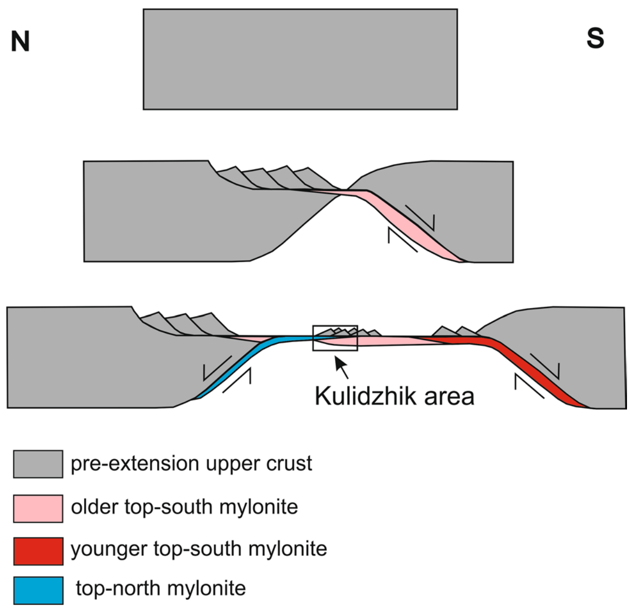

Fig. 13 Sketch of the Late Eocene kinematic evolution of extensional fault systems in the Eastern Rhodopes. Extension started asymmetric with a south-dipping detachment system (middle section) and went on symmetric with two outward-dipping detachment systems (lower section). In the Kulidzhik area, Unit I shows top-to-the south mylonites (*pink*) overprinted by top-to-the north shearing, whereas Unit II and III show only top-to-the north mylonite (*blue*). Unit IV is an extensional klippe on the detachment system (*grey*). Earlier thrusting-related structures are not shown here

top-south mylonites in Unit I formed in this large-scale shear zone. The unloaded footwall started to evolve into a metamorphic core complex. In an advanced stage of extension, an antithetic, top-north shear zone nucleated on the up-dip side of the core complex and developed into the Kulidzhik detachment. From now on, the extension and unroofing of the metamorphic core of the Eastern Rhodopes went on in a symmetrical manner. In the Kulidzhik area, this led to the observed overprinting relations. Such nucleation of an antithetic, top-northeast detachment (Dobrotino Fault) on the up-dip side of an evolving core complex has also been shown by Georgiev et al. (2010) for the Pirin Mountains.

Alternatively, it is also possible that in an early stage, top-south shearing at a lower crustal level was coeval with top-north shearing at a higher level, i.e. the thickened orogenic crust was thinned by conjugate shear zones as observed in passive continental margins (e.g. Brun and Beslier 1996; Nagel and Buck 2004; Froitzheim et al. 2006) and in areas of postorogenic extension like the Devonian-age Caledonides (Fossen et al. 2014). More precise cooling-age dating would be necessary to distinguish between these options.

Conclusions

Our structural, petrographic, and geochronological study allowed to correlate the tectonic units of the Kulidzhik River valley with major tectonic elements of the Rhodope Metamorphic Complex. Unit I is mainly orthogneiss, formed from Late Variscan granite (ca. 300 Ma), as is typical for the Lower Allochthon of the Rhodopes.

Garnet-bearing mica schists from Unit II were formed from Permian or Early Mesozoic clastic sediments bearing detrital, mainly Late Variscan (310–250 Ma) zircons. These rocks were affected by high-grade (granulite-facies) metamorphism in the Jurassic (ca. 150 Ma) and a second time in the Late Cretaceous (69 Ma). Unit II is equivalent to the Krumovitsa-Kimi Unit (Upper Allochthon).

Low-grade metamorphic greenschist, phyllite, and calcschist of Unit III represent the Uppermost Allochthon or Circum-Rhodope Belt. The muscovite-rich, leucocratic orthogneiss of Unit IV formed from a Proterozoic (ca. 581 Ma) granite and was metamorphosed before the Jurassic, as shown by published ^{39}Ar–^{40}Ar muscovite cooling ages of ca. 154 and ca. 157 Ma (Bonev et al. 2010a).

These units were deformed and variably retrograded by Eocene-age extensional shearing and detachment faulting. The newly defined, top-north Kulidzhik Detachment is represented by a near-surface, kakiritic detachment fault along the base of Unit IV, a second detachment fault with chlorite-rich cataclasites at the top of Unit II, as well as top-north, lower greenschist facies mylonites in Units I, II, and III. The dominant fabric in Unit I, however, is related to the top-south mylonitic shearing under decreasing temperatures, starting in the higher greenschist or amphibolite facies. These structures probably represent the transition from asymmetric (top-south) extensional unroofing to symmetric, bivergent unroofing, accommodated by the top-southwest Kechros Detachment to the south and the top-north Kulidzhik Detachment along the northern border of the Eastern Rhodopes.

Acknowledgments This article is dedicated to the memory of late Professor Zivko Ivanov who inspired generations of geologists to work on the Rhodope geology. We are grateful to Alexandre Kounov and Albrecht von Quadt for their constructive reviews which considerably helped to improve this article.

References

Arkadakskiy S, Böhm C, Heaman L, Cherneva Z, Stancheva E, Ovtcharova M (2003) Remnants of Neoproterozoic oceanic crust in the Central Rhodope metamorphic complex, Bulgaria. In: The geological society of America Vancouver annual meeting, GS3-62

Bauer C, Rubatto D, Krenn K, Proyer A, Hoinkes G (2007) A zircon study from the Rhodope metamorphic complex, N-Greece: time record of a multistage evolution. Lithos 99:207–228
Bonev N (2004) Sillimanite-bearing migmatites from the Rhodope metamorphic complexes, southern Bulgaria: occurrence and implications for the tectono-metamorphic history. Neues Jb Geol Paläont Abh 229:57–75
Bonev N (2006a) Structural and geochemical studies on amphibolites and greenschist-facies rocks in the Kulidjik river valley, eastern Rhodope, Bulgaria: preliminary results. Neues Jb Geol Paläont Abh 239:161–181
Bonev N (2006b) Cenozoic tectonic evolution of the eastern Rhodope massif (Bulgaria): basement structure and kinematics of syn- to postcollisional extensional deformation. In: Dilek Y, Pavlides S (eds) Postcollisional tectonics and magmatism in the Mediterranean region and Asia. Geol Soc Am Spec Pap 409:211–235
Bonev N, Burg J-P, Ivanov Z (2006a) a) Mesozoic-Tertiary structural evolution of an extensional gneiss dome—the Kesebir-Kardamos dome, eastern Rhodope (Bulgaria-Greece). Int J Earth Sci 95:318–340
Bonev N, Marchev P, Singer B (2006b) b) $^{40}Ar/^{39}Ar$ geochronology constraints on the Middle Tertiary basement extensional exhumation and its relation to ore-forming and magmatic processes in the Eastern Rhodope (Bulgaria). Geodin Acta 19:267–282
Bonev N, Spiking R, Moritz R, Marchev P (2010a) The effect of Alpine thrusting in late-stage extensional tectonics: evidence from the Kulidzhik nappe and the Pelevun extensional allochthon in the Rhodope Massif, Bulgaria. Tectonophysics 488:256–281
Bonev N, Spiking R, Moritz R, Marchev P (2010b) Timing of extensional exhumation of the Eastern Rhodope high-grade basement (Bulgaria): $^{40}Ar/^{39}Ar$ age constraints. In: National conference GEOSCIENCE proceedings, Sofia, pp 117–118
Bonev N, Moritz R, Márton I, Chiaradia M, Marchev P (2010c) c) Geochemistry, tectonics, and crustal evolution of basement rocks in the Eastern Rhodope Massif, Bulgaria. Int Geol Rev 52:269–297
Bonev N, Marchev P, Moritz R, Collings D (2015) Jurassic subduction zone tectonics of the Rhodope Massif in the Thraceregion (NE Greece) as revealed by new U–Pb and $^{40}Ar/^{39}Ar$ geochronology of the Evros ophiolite and high-grade basement rocks. Gondwana Res 27:760–775
Bosse V, Boulvais P, Gautier P, Tiepolo M, Ruffet J, Devidal L, Cherneva Z, Gerdjikov I, Paquette JL (2009) Fluid-induced disturbance of the monazite Th-Pb chronometer: in situ dating and element mapping in pegmatites from the Rhodope (Greece, Bulgaria). Chem Geol 261:286–302
Boyanov I (1969) Notes sur la nappe de Koulidjik. Bulg Acad Sci Bull Geol Inst Ser Geotect 18:159–165 **(in Bulgarian, abstract in French)**
Boyanov I, Lipman P (1973) On the Lower Cretaceous age of the low-crystalline metamorphic complex in the East Rhodopes. C R Acad Bulg Sci 26:1225–1226 **(in Russian, abstract in English)**
Boyanov I, Kozhouharova E, Kozhouharov D (1969) Relationships between the Pre Cambrian high-crystalline base and the Diabasephylitoid Formation in the Eastern Rhodope. Rev Bulg Geol Soc 30(2):113–122 **(in Bulgarian, abstract in English)**
Boyanov I, Ruseva M, Toprakcieva V, Dimitrova E (1990) Lithostratigraphy of the Mesozoic rocks from the Eastern Rhodopes. Geol Balc 20:3–28 **(in Russian, abstract in English)**
Brun J-P, Beslier M-O (1996) Mantle exhumation at passive margins. Earth Planet Sci Lett 142:161–173
Brun J-P, Sokoutis D (2007) Kinematics of the Southern Rhodope Core Complex (North Greece). Int J Earth Sci 96:1079–1099
Burchfiel BC, Nakov R, Tzankov T (2003) Evidence from the Mesta half-graben, SW Bulgaria, for the Late Eocene beginning of Aegean extension in the Central Balkan Peninsula. Tectonophysics 375:61–76
Burg J-P (2012) Rhodope: from Mesozoic convergence to Cenozoic extension. Review of petro-structural data in the geochronological frame. J Virtual Explor. doi:10.3809/jvirtex.2011.00270
Burg J-P, Ivanov Z, Ricou L-E, Dimov D, Klain L (1990) Implications of shear-sense criteria for the tectonic evolution of the Central Rhodope Massif, southern Bulgaria. Geology 18:451–454
Burg J-P, Ricou L-E, Ivanov Z, Godfriaux I, Dimov D, Klain L (1996) Syn-metamorphic nappe complex in the Rhodope Massif. Structure and kinematics. Terra Nova 8:6–15
Carrigan CW, Mukasa SB, Haydoutov I, Kolcheva K (2003) Ion microprobe U–Pb zircon ages of pre-Alpine rocks in the Balkan, Sredna Gora, and Rhodope Terranes of Bulgaira: constraints on Neoproterozoic and Variscan tectonic evolution. J Czech Geol Soc 48:32–33
Cherneva Z, Ovtcharova M, Arkadakskiy S, von Quadt A, Peytcheva I (2003) Accessory minerals behavior during Eocene melting of Hercynian granitoids in the Central Rhodope Dome, Bulgaria. Final GEODE-ABCD Workshop, Seggauberg, Austria, pp 25–26
Connolly JAD (2005) Computation of phase equilibria by linear programming: a tool for geodynamic modeling and its application to subduction zone decarbonation. Earth Planet Sc Lett 236:524–541
Dixon J, Dimitriadis S (1984) Metamorphosed ophiolitic rocks from the Serbo-Macedonian Massif, near Lake Volvi, north-east Greece. In: Dixon JE, Robertson AHF (eds) The geological evolution of the eastern mediterranean. Geol Soc Spec Publ 17:603–618
Dimov D, Dobrev S, Ivanov Z, Kolkovski B, Sarov S (2000) Structure, Alpine evolution and mineralizations of the Central Rhodopes area (South Bulgaria). In: Ivanov Z (ed) ABCD-GEODE workshop, Gidebook to excursion B. Borovets, Bulgaria, p 50
Dinter DA (1998) Late Cenozoic extension of the Alpine collisional orogen, northeastern Greece: origin of the north Aegean basin. Geol Soc Am Bull 110:1208–1226
Ferry JM, Watson EB (2007) New thermodynamic models and revised calibrations for the Ti-in-zircon and Zr-in-rutile thermometers. Contrib Mineral Petrol 154:429–437
Fossen H, Gabrielsen RH, Faleide JI, Hurich CA (2014) Crustal stretching in the Scandinavian Caledonides as revealed by deep seismic data. Geology 42:791–794
Froitzheim N, Pleuger J, Nagel TJ (2006) Extraction faults. J Struct Geol 28:1388–1395. doi:10.1016/j.jsg.2006.05.002
Froitzheim N, Jahn-Awe S, Frei D, Wainwright AN, Maas R, Georgiev N, Nagel TJ, Pleuger J (2014) Age and composition of meta-ophiolite from the Rhodope Middle Allochthon (Satovcha, Bulgaria): a test for the maximum-allochthony hypothesis of the Hellenides. Tectonics. doi:10.1002/2014TC003526
Gautier P, Gerdjikov I, Ruffet G, Bosse V, Cherneva Z, Pitra P, Hallot E (2010). Persistent synmetamorphic thrusting in the Rhodope until 33 Ma: evidence from the Nestos Shear Zone and implications for Aegean geodynamics. In: XIX Congress of the Carpathian Balkan geological association, Thessaloniki, Greece, 23–26 September 2010, abstract volume 122–123
Georgiev N, Pleuger J, Froitzheim N, Sarov S, Jahn-Awe S, Nagel TJ (2010) Separate Eocene-Early Oligocene and Miocene stages of extension and core complex formation in the Western Rhodopes, Mesta Basin, and Pirin Mountains (Bulgaria). Tectonophysics 487:59–84
Gerdjikov I, Gautier P (2005) Early Alpine orogeny as recorded in the metamorphic complexes of Southern Bulgaria. EGU General Assembly 2005, abstracts, vol 7, EGU05-A-11126
Gerdjikov I, Gautier P, Cherneva Z, Bosse V, Ruffet G (2010) Late Eocene synmetamorphic thrusting and syn-orogenic extension across the metamorphic pile of the Bulgarian Central Rhodope.

In: XIX Congress of the Carpathian Balkan geological association, Thessaloniki, Greece, 23–26 September 2010, abstract volume 132–133
Himmerkus F, Reischmann T, Kostopoulos D (2006) Late Proterozoic and Silurian basement unitswithin the Serbo-Macedonian Massif, northern Greece: the significance of terrane accretion in the Hellenides. In: Robertson AHF, Mountrakis D (eds) Tectonic development of the Eastern Mediterranean Region. Geol Soc Spec Publ 260:35–50
Hoskin P, Schaltegger U (2003) The Composition of Zircon and Igneous and Metamorphic Petrogenesis. Rev Mineral Geochem 53(1):27–62
Ivanov Z (1989) Structure and tectonic evolution of the central parts of the Rhodope massif. In: Ivanov Z (ed) Guide to excursion E-3, CBGA-XIV congress, Sofia, Bulgaria, p 126
Ivanov Z (1998) Tectonics of Bulgaria. Professorship Thesis (in Bulgarian)
Jackson S, Pearson N, Griffin W, Belousova E (2004) The application of laser ablation-inductively coupled plasma-mass spectrometry to in situ U–Pb zircon geochronology. Chem Geol 211:47–69
Jahn-Awe S, Froitzheim N, Nagel TJ, Frei D, Georgiev N, Pleuger J (2010) Structural and geochronological evidence for Paleogene thrusting in the Western Rhodopes, SW Bulgaria: elements for a new tectonic model of the Rhodope Metamorphic Province. Tectonics 29:TC3008. doi:10.1029/2009TC002558
Janák M, Froitzheim N, Georgiev N, Nagel TJ, Sarov S (2011) P-T evolution of kyanite eclogite from the Pirin Mountains (SW Bulgaria): implications for the Rhodope UHP Metamorphic Complex. J Metamorph Geol 29:317–332
Jaranoff D (1960) La tectonique de la Bulgarie. Sofia, Technica (in Bulgarian, abstract in French)
Kauffmann G, Kockel F, Mollat H (1976) Notes on the stratigraphic and paleogeographic position of the Svoula Formation in the innermost zone of the Hellenides (Northern Greece). Bull Soc Geol Fr 18:225–230
Kilias A, Falalakis G, Mountrakis D (1999) Cretaceous-Tertiary structures and kinematics of the Serbomacedonian metamorphic rocks and their relation to the exhumation of the Hellenic hinterland (Macedonia, Greece). Int J Earth Sci 88:513–531
Kirchenbaur M, Pleuger J, Jahn-Awe S, Nagel TJ, Froitzheim N, Fonseca ROC, Münker C (2012) Timing of high-pressure metamorphic events in the Bulgarian Rhodopes from Lu-Hf garnet geochronology. Contrib Mineral Petr 163:897–921
Krohe A, Mposkos E (2002) Multiple generations of extensional detachments in the Rhodope Mountains (northern Greece): evidence of episodic exhumation of high-pressure rocks. In: Blundell DJ, Neubauer F, von Quadt A (eds) The timing and location of major ore deposits in an evolving Orogen. Geol Soc London Sp Publ 204:151–178
Liati A (2005) Identification of repeated Alpine (ultra) high-pressure metamorphic events by U–Pb SHRIMP geochronology and REE geochemistry of zircon: the Rhodope zone of Northern Greece. Contrib Mineral Petr 150:608–630
Liati A, Gebauer D (1999) Constraining the prograde and retrograde P-T-t path of Eocene HP rocks by SHRIMP dating of different zircon domains: inferred rates of heating, burial, cooling and exhumation for central Rhodope, northern Greece. Contrib Mineral Petrol 135:340–354
Liati A, Gebauer D, Wysoczanski R (2002) U–Pb SHRIMP-dating of zircon domains from UHP garnet-rich mafic rocks and late pegmatoids in the Rhodope zone (N Greece); evidence for Early Cretaceous crystallization and Late Cretaceous metamorphism. Chem Geol 184:281–299
Liati A, Gebauer D, Fanning CM (2011) Geochronology of the Alpine UHP Rhodope Zone: a review of isotopic ages and constraints on the geodynamic evolution. In: Dobrzhinetskaya LF, Faryad SW, Wallis S, Cuthbert S (eds) Ultrahigh-pressure metamorphism. Elsevier, Amsterdam, pp 295–324
Liati A, Theye T, Fanning CM, Gebauer D, Rayner N (2015) Multiple subduction cycles in the Alpine orogeny, as recorded in single zircon crystals (Rhodope zone, Greece). Gondwana Res. doi:10.1016/j.gr.2014.11.007
Lips ALW, White SH, Wijbrans JR (2000) Middle-Late Alpine thermotectonic evolution of the southern Rhodope Massif, Greece. Geodin Acta 13:281–292
Macheva LA (1998) 3T-phengites in the rocks from the ByalaReka metamorphic group: an indicator of high-pressure metamorphism. Geochem Mineral Petrol 35:17–28
Marchev P and Singer B (2002) $^{40}Ar/^{39}Ar$ geochronology of magmatism and hydrothermal activity of the Madjarovo base-precious metal ore district, eastern Rhodopes, Bulgaria. In: Blundell DJ, Neubauer F, von Quadt A (eds) The timing and location of major ore deposits in an evolving Orogen. Geological Society of London Special Publication 204:137–150
Marchev P, von Quadt A, Peytcheva I, Ovtcharova I (2006) The age and origin of the Chuchuliga and Rozino granites, Eastern Rhodopes. In: National conference GEOSCIENCE proceedings, Sofia 2006, pp 213–216
Michard A, Goffe B, Liati A, Mountrakis D (1994) Blueschist-facies assemblages in the peri-Rhodopian zone and hints for an Eohellenic HP/LT belt in northern Greece. Bull Soc Geol Greece 30:185–192
Mposkos ED (1989) High-pressure metamorphism in gneisses and pelitic schists in the East Rhodope Zone (N. Greece). Mineral Petrol 41:25–39
Mposkos ED, Kostopoulos DK (2001) Diamond, former coesite and supersilicic garnet in metasedimentary rocks from the Greek Rhodope: a new ultrahigh-pressure metamorphic province established. Earth Planet Sci Lett 192:497–506
Mukasa SB, Haydoutov I, Carrigan CW, Kolcheva K (2003) Thermobarometry and $^{40}Ar/^{39}Ar$ ages of eclogitic and gneissic rocks in the Sredna Gora and Rhodope terranes of Bulgaria. J Czech Geol Soc 48:94–95
Nagel TJ, Buck WR (2004) Symmetric alternative to asymmetric rifting models. Geology 32:937–940
Nagel TJ, Schmidt S, Janák M, Froitzheim N, Jahn-Awe S, Georgiev N (2011) The exposed base of a collapsing wedge—the Nestos Shear Zone (Rhodope Metamorphic Province, Greece). Tectonics 30:TC4009. doi:10.1029/2010TC002815
Ovtcharova M, Cherneva Z, von Quadt A, Peytcheva I (2002) Migmatitic geochronology and geochemistry—a key to understanding the exhumation of the Madan Dome (Bulgaria). Geochim Cosmochim Acta 66(Supplement 1):573
Perraki M, Proyer A, Mposkos E, Kaindl R, Hoinkes G (2006) Raman micro-spectrometry on diamond, graphite and other carbon polymorphs from the ultrahigh-pressure metamorphic Kimi Complex of the Rhodope Metamorphic Province, NE Greece. Earth Planet Sci Lett 241:672–685
Peytcheva I, von Quadt A (1995) U–Pb zircon dating ofmetagranites-fromByalaReka regionin the east Rhodopes, Bulgaria. Geol Soc Greece Spec Publ 4:637–642
Peytcheva I, Bibikova EV, Makarov V (1992) U–Pb dating of zircons from two types of gneisses from the Southeastern Rhodopes of Bulgaria. C R Bulg Acad Sci 45(8):71–74
Peytcheva I, Ovtcharova M, Sarov S, Kostitsin J (1998) Age and metamorphic evolution of metagranitoids from Kesebirreka region, Eastern Rhodopes: Rb–Sr isotope data. In: XVI Congress of the CBGA, Vienna, abstracts 471
Peytcheva I, von Quadt A, Ovtcharova M, Handler R, Neubauer F, Salnikova E, Kostitsyn Y, Sarov S, Kolcheva K (2004) Metagranitoids from the eastern part of the Central Rhodopean Dome (Bulgaria): U–Pb, Rb–Sr and $^{40}Ar/^{39}Ar$ timing of emplacement

and exhumation and isotope-geochemical features. Mineral Petrol 82:1–31. doi:10.1007/s00710-004-0039-3

Pleuger J, Georgiev N, Jahn-Awe S, Froitzheim N, Valkanov N (2011) Kinematics of Palaeogene low-angle extensional faults and basin formation along the eastern border of the Central Rhodopes (Bulgaria). Z Dtsch Ges Geowiss 162:171–192

Ricou LE, Burg JP, Godfriaux I, Ivanov Z (1998) Rhodope and Vardar: the metamorphic and the olistostromic paired belts related to the Cretaceous subduction under Europe. Geodin Acta 11:285–309

Rubatto D (2002) Zircon trace element geochemistry: partitioning with garnet and the link between U–Pb ages and metamorphism. Chem Geol 184:123–138

Sarov S, Yordanov B, Georgiev S, Valkov V, Balkanska E, Grozdev V, Marinova R, Markov N (2007) Map sheets K-35-88-V (Krumovgrad) and K-35-100-A (Egrek). Explanatory note to the Geological map of the Republic of Bulgaria scale 1:50,000, p 104

Sarov S, Yordanov B, Georgiev S, Valkov V, Balkanska E, Grozdev V, Marinova R, Markov N (2008) Map sheet K-35-88-B (Madzharovo). Explanatory note to the Geological map of the Republic of Bulgaria scale 1:50,000, p 100

Sarov S, Voinova E, Ovtcharova M, Naydenov K, Georgiev N, Dimov D (2010) Lithotectonic subdivision of the metamorphic rocks in Rila-Rhodope region. In: National conference GEOSCIENCE proceedings, Sofia 2010, p 121

Schmidt S, Nagel TJ, Froitzheim N (2010) A new location with micro-diamond-bearing metamorphic rocks south of Sidironero (SW Rhodopes/Greece). Eur J Mineral 22:189–198. doi:10.1127/0935-1221/2010/0022-1999

Shipkova K, Ivanov Z (2000) The Djerman Detachment fault—an effect of the late Tertiary extension in the north-west part of the Rhodope Massif. C R Acad Bulg Sci 53(2):81–84

Simpson GDH, Thompson AB, Connolly JAD (2000) Phase relations, singularities and thermobarometry of metamorphic assemblages containing phengite, chlorite, biotite, K-feldspar, quartz and H2O. Contrib Mineral Petrol 139:555–569

Stacey JS, Kramers JD (1975) Approximation of terrestrial lead isotope evolution by a 2-stage model. Earth Planet Sci Lett 26(2):207–221

Stipp M, Stünitz H, Heilbronner R, Schmid SM (2002) The eastern Tonale fault zone: a “natural laboratory” for crystal plastic deformation of quartz over a temperature range from 250 to 700 °C. J Struct Geol 24:1861–1884

Tikhomirova L, Boyanov I, Zagorčev I (1988) Early Jurassic Radiolarians from the Eastern Rhodopes: a revision of the age of Dolno-Lukovo Formation. Geol Balc 18(6):58

Tueckmantel C, Schmidt S, Neisen M, Georgiev N, Nagel TJ, Froitzheim N (2008) The Rila-Pastra Normal Fault and multi-stage extensional unroofing in the Rila Mountains (SW Bulgaria). Swiss J Geosci 101:295–310

Turpaud P, Reischmann T (2010) Characterisation of igneous terranes by zircon dating: implications for UHP occurrences and suture identification in the Central Rhodope, northern Greece. Int J Earth Sci 99:567–591

von Quadt A, Peytcheva I (1995) U–Pb zircon ages of metagranites from the Byala-Reka-region—evidence for a Variscian orogen in the Rhodopes. Terra Nostra, Potsdam, Oct. 1995, pp 103–105

Wain A, Waters D, Jephcoat A, Olijynk H (2000) The high-pressure to ultrahigh-pressure eclogite transition in the Western Gneiss Region, Norway. Eur J Mineral 12:667–687